Charge Recombination and Protein Dynamics in Bacterial Photosynthetic Reaction Centers Entrapped in a Sol-Gel Matrix

Jan M. Kriegl,* Florian K. Forster,* and G. Ulrich Nienhaus*†
*Department of Biophysics, University of Ulm, Ulm, Germany; and †Department of Physics, University of Illinois at Urbana-Champaign, Urbana, Illinois

ABSTRACT Many proteins can be immobilized in silica hydrogel matrices without compromising their function, making this a suitable technique for biosensor applications. Immobilization will in general affect protein structure and dynamics. To study these effects, we have measured the $P^+Q_A^-$ charge recombination kinetics after laser excitation of Q_B-depleted wild-type photosynthetic reaction centers from *Rhodobacter sphaeroides* in a tetramethoxysilane (TMOS) sol-gel matrix and, for comparison, also in cryosolvent. The nonexponential electron transfer kinetics observed between 10 and 300 K were analyzed quantitatively using the spin boson model for the intrinsic temperature dependence of the electron transfer and an adiabatic change of the energy gap and electronic coupling caused by protein motions in response to the altered charge distributions. The analysis reveals similarities and differences in the TMOS-matrix and bulk-solvent samples. In both preparations, electron transfer is coupled to the same spectrum of low frequency phonons. As in bulk solvent, charge-solvating protein motions are present in the TMOS matrix. Large-scale conformational changes are arrested in the hydrogel, as evident from the nonexponential kinetics even at room temperature. The altered dynamics is likely responsible for the observed changes in the electronic coupling matrix element.

INTRODUCTION

Both natural and engineered proteins have great potential as exquisitely selective, versatile catalysts and recognition elements in many different applications in scientific areas such as synthetic and analytical chemistry, medicine, biotechnology, bioremediation, and environmental monitoring. Often, technical applications demand efficient ways of immobilizing proteins. For instance, industrial bioconversion processes require high-density, heterogeneous catalysts, permitting high activities over extended time periods while tolerating a range of operating conditions. Biosensors and biochips are frequently based on precisely engineered architectures, containing immobilized biomolecules in their fully functional conformation (Gill and Ballesteros, 2000a,b).

Various ways have been devised to form bioimmobilizates, such as covalent binding to solid surfaces and supported organic films, entrapment in polymer hydrogels, and microencapsulation. A particularly attractive approach promising wide applicability appears to be the formation of biomolecule-polymer composites in which biomolecules are permanently entrapped within covalent polymer networks (Gill and Ballesteros, 2000a,b). Recent years have seen enormous progress in the sol-gel encapsulation of biomolecules in porous silica networks. By modification of the classic sol-gel methods, mild polymerization conditions were developed so that proteins maintain their native structure and characteristic activities when co-polymerized with the silica matrix (Ellerby et al., 1992). The polymer matrices thus produced were shown to be permeable enough to enable diffusion of lower weight substrates while retaining even smaller proteins in the mass range ~10 kD. A large variety of novel biosensors has been developed based on encapsulation of biomolecules in silica sol-gel matrices, with applications ranging from the detection of small amounts of gaseous molecules such as O_2, CO, or NO to the determination of glucose content in liquids (Gill and Ballesteros, 1998, 2000a; Tess and Cox, 1999; Livage et al., 2001).

As of yet, little is known about the structural details of the biomolecule-matrix interaction. Protein function is intimately linked to the ability of the protein to perform structural fluctuations among many different conformational substates (Frauenfelder et al., 1991; Nienhaus and Young, 1996). Consequently, the details of the biomolecule-matrix interaction determine if an encapsulated protein will be completely, partly, or not at all functional when embedded in the polymer matrix. Spectroscopic and electrochemical studies on a number of proteins in silica hydrogels and xerogels (Gill and Ballesteros, 1998, 2000a; Livage et al., 2001) have suggested that the proteins are entrapped in their native conformation in tight cages, so that rotations and global conformational changes are restricted, but local motions required for substrate binding and catalysis are still possible. For instance, hemoglobins can be trapped in their different quaternary (R,T) states in the gel, and the polymer matrix suppresses global R-T interconversions entirely (Shibayama and Saigo, 1995; Khan et al., 2000, 2001). These studies showed unambiguously that large-scale dynamics of biomolecules is strongly hindered in the glassy cage. However, the origin of the forces restricting global protein motions is still unknown. Besides the obvious

Submitted December 31, 2002, and accepted for publication May 19, 2003.
Address reprint requests to Gerd Ulrich Nienhaus, Dept. of Biophysics, University of Ulm, 89069 Ulm, Germany. Tel.: 49-731-502-3050; Fax: 49-731-502-3059; E-mail: uli@uiuc.edu.

0006-3495/03/09/1851/20 $2.00

mechanical effects, specific electrostatic interactions between silicate sites and protein surface residues have been proposed to influence the flexibility of the protein (Shibayama and Saigo, 1995; Livage et al., 2001; Gottfried et al., 1999).

In this work, we have examined how encapsulation in a silica sol-gel matrix affects the kinetics of light-induced long-range electron transfer (ET) in reaction centers (RCs) of photosynthetic purple bacteria (*Rhodobacter sphaeroides*). RCs are membrane-bound pigment-protein complexes that consist of three polypeptide subunits (H, L, and M) and a number of cofactors. ET occurs by sequential electron tunneling between the cofactors, and even slight modifications of their mutual coupling can give rise to substantial variations of ET rates (Marcus and Sutin, 1985; Moser et al., 1992; Dutton and Mosser, 1994; Moser et al., 1995; Gray and Winkler, 1996; Page et al., 1999). This sensitivity enables us to examine the influence of the protein environment on the ET reaction by precise measurements of the ET kinetics. Light absorption initially causes promotion of the electronic system of the special pair (P), a bacteriochlorophyll dimer located close to the periplasmatic side of the membrane, to its first excited singlet state (P^*). Subsequently, the electron is transferred within 4 ps via an accessory bacteriochlorophyll to a bacteriopheophytin (H_A) and within another 200 ps further to the primary acceptor, a ubiquinone UQ_{10} (Q_A), which is located 25 Å away from the special pair, close to the cytoplasmatic side of the protein (Allen et al., 1987; Feher et al., 1989; Ermler et al., 1994). The final, secondary acceptor (Q_B) takes up two electrons and two protons, leaves its binding pocket and delivers the electrons and protons to the bc_1 complex (Feher et al., 1989; Hoff and Deisenhofer, 1997). In the preparations that we have used for this study, the secondary quinone (Q_B) was removed so that the electron recombines with the hole on the special pair, thus restoring the RC within ≈120 ms (room temperature) back to its ground state,

$$PH_AQ_A \xrightarrow{h\nu} P^*H_AQ_A \rightarrow P^+H_A^-Q_A \rightarrow P^+H_AQ_A^- \rightarrow PH_AQ_A. \quad (1)$$

The last and slowest ET step in the sequence, $P^+Q_A^- \rightarrow PQ_A$ (because the pheophytin is not involved in this particular ET step, we drop the H for simplicity), is particularly attractive for detailed, quantitative studies. It is long-ranged, and the large spatial separation leads to weak coupling of the donor and acceptor electronic states, which ensures nonadiabatic ET from a thermally equilibrated initial manifold of vibrational states.

To assess how protein motions affect the ET reaction, we use the sample temperature as our key control variable. There are two ways in which temperature affects ET:

1. The intrinsic temperature dependence arises from the coupling of the ET reaction to the phonon bath. Here we use the spin boson model (Leggett et al., 1987; Warshel et al., 1989; Xu and Schulten, 1992, 1994) to describe the observed, nonexponential kinetics and its temperature dependence. To achieve this, we introduce distributions of energy gaps and electronic coupling elements between donor and acceptor states to account for structural heterogeneity in the sample.
2. An extrinsic temperature (and time) dependence arises from light-induced charge separation. The electric field changes substantially perturb the protein and give rise to conformational changes (Noks et al., 1977; Kleinfeld et al., 1984; Woodbury and Parson, 1986; Rubin et al., 1994; Peloquin et al., 1994). They in turn adiabatically influence the key physical parameters and thus the ET kinetics.

The basic strategy with which we exploit the extrinsic temperature dependence to gain insight into the coupling of ET and protein motions can be understood with the schematic in Fig. 1, depicting free energy surfaces of the $P^+Q_A^-$ and PQ_A electronic states as a function of a conformational coordinate q. They are assumed to be overall parabolic but exhibit a certain ruggedness, as can be inferred from the temperature dependence of the observed protein motions. Within the Condon approximation, transitions between the charge-separated and neutral states are vertical in this scheme. The energy gap, ε, the vertical separation between the two surfaces, is the crucial physical

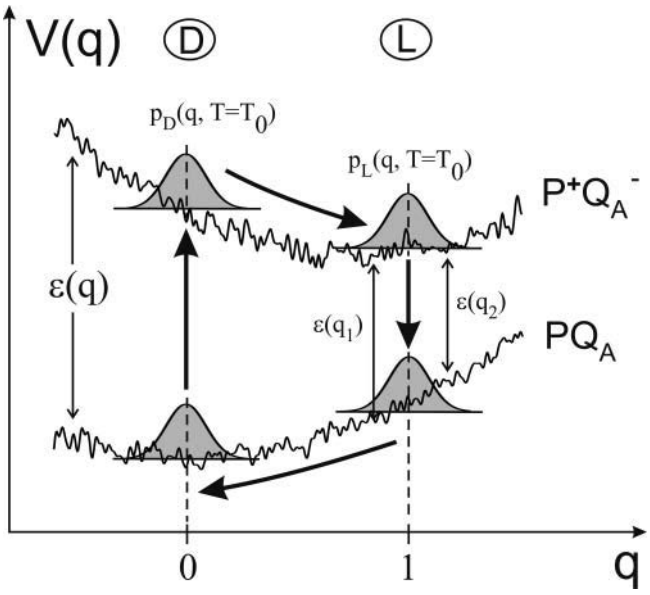

FIGURE 1 Schematic representation of the energy surfaces in the neutral (PQ_A) and charge-separated($P^+Q_A^-$) states of RCs, showing how the energy gap ε, which controls the ET rates, varies as a function of conformational coordinate q. Samples cooled in the dark (dark-adapted, D) are characterized by a conformational distribution at $q \approx 0$, samples cooled under illumination from room temperature (light-adapted, L) are centered at $q \approx 1$. Note the different energy gaps present within the distribution. Relaxations occur on both energy surfaces; the arrows indicate the cycle that a protein undergoes upon charge separation at room temperature.

parameter governing the ET rate. As it is evident from Fig. 1, ε varies with q, and therefore, the evolution of the protein ensemble on the lower or upper energy surfaces can be studied by measuring the charge recombination kinetics.

In the experiment, samples are either cooled in the dark, or a strong light source is switched on during cooling at several temperatures T_L, keeping the RCs in the charge-separated state. After arrival at 10 K, we measure light-induced ET kinetics while slowly increasing the temperature from 10 to 300 K over a period of several hours. Upon cooling in the dark, the RCs are frozen in the neutral PQ_A state, and the ensemble of RCs is distributed around the minimum of the lower energy surface ($q = 0$ in Fig. 1). For simplicity, we shall refer to this as the dark-adapted conformation (D). Light excitation pitchforks the molecules onto the upper surface, where they stay for a few milliseconds before recombination. At 10 K, the ruggedness of the surface is too large, and the RCs will not change conformational coordinate during their brief residence on the $P^+Q_A^-$ surface (Fig. 1). As temperature increases, thermally activated transitions on the upper surface become possible, and the ensemble can progress toward the minimum at $q = 1$, which we refer to as the light-adapted conformation (L). This motion is accompanied by an energy gap decrease. The theoretical analysis then yields a concomitant decrease of the ET rate.

By exposing the samples to a strong light source while cooling from room temperature to 10 K, samples will essentially be kept in the charge-separated state, and will be arrested in the light-adapted conformation ($q = 1$). After switching off the light at 10 K, a distribution of molecules has been prepared on the PQ_A surface at $q \approx 1$ that cannot relax toward $q = 0$ because of the ruggedness of the energy landscape. As the temperature is slowly raised over several hours, energy barriers can be overcome, and the ensemble slowly moves to the left. During this relaxation, we can propel the molecules to the upper surface by laser excitation and measure their position along q via the ET kinetics.

In an earlier study, we had measured the kinetics of charge recombination from the primary acceptor in RCs of the carotenoid-deficient strain R26 of *Rb. sphaeroides* dissolved in glycerol-water mixtures and presented a detailed quantitative picture of the coupling between ET and protein motions solvating the altered charge distribution (McMahon et al., 1998). Here we use this strategy to assess the effect of encapsulation of (carotenoid containing) RCs in a sol-gel matrix on the protein motions accompanying ET in the proteins.

MATERIALS AND METHODS

Bacteria growth and RC purification

For this study, we have used RC proteins with engineered poly-His tag (Goldsmith and Boxer, 1996). Bacteria were grown anaerobically under illumination in 2 liters of YCC medium at 34°C for six days, yielding 5 g cells/l of medium (fresh weight) (Clayton and Sistrom, 1978). The cells were harvested at 4°C by centrifugation and kept at −80°C for long-term storage. After thawing, the cells were resuspended in lysis buffer (10 mM Tris, 100 mM NaCl, pH 8.0) and stirred for 30 min at room temperature (Goldsmith and Boxer, 1996). Lysozyme (Sigma-Aldrich Chemie GmbH, Munich, Germany), was added to a final amount of 0.8 mg/g cells (fresh weight) to break the cell membranes. The suspension was stirred for 30 min at 4°C and, after addition of deoxycholic acid (4 mg/g cells), heated to 37°C for 10 min. Subsequently, DNase (≈20 μg/g cells, Sigma-Aldrich Chemie GmbH, Munich, Germany) was added, and the lysate was stirred for yet another 30 min at room temperature. Lysate and cell debris were separated by centrifugation at 15,000 rpm (rotor SS-34, Sorvall, Newtown, CT) for 15 min. After collecting the supernatant, we essentially followed the purification protocol reported by Goldsmith and Boxer (1996). 0.5% (v/v) LDAO (Fluka, Buchs, Switzerland) and 5 mM imidazole and, thereafter, Ni-NTA resin (Qiagen GmbH, Hilden, Germany), equilibrated in purification buffer (10 mM Tris, 0.1% (v/v) LDAO, pH 8.0), was added to the solution. After gentle stirring at 4°C overnight, the slurry was poured onto an empty column. The poly-His RCs were eluted using 100 mM imidazole in purification buffer. Removal of the imidazole, further purification and concentration was achieved by gel filtration (Sephadex G25 column, Amersham Biosciences Europe GmbH, Freiburg, Germany) and Amicon filtration (molecular weight cutoff 100 kD). For removal of the secondary quinone, Q_B, RCs were loaded on a Toyopearl DEAE 650S anion exchange column (TosoHaas GmbH, Stuttgart, Germany) and washed with inhibition buffer (0.5 mM 1,10-phenanthroline, 10 mM Tris, 1% (v/v) LDAO; Okamura et al., 1975). The extent of Q_B removal was checked via the decay of the $P^+H_A^-$ triplet state which appears in RCs that have lost both Q_B and the more strongly bound primary quinone Q_A (Volk et al., 1995).

Sample preparation

Purified and Q_B-extracted RCs were dissolved in a mixture of 75% glycerol and 25% buffer (10 mM Tris, 0.1% (v/v) LDAO, pH 8.0) to a final concentration of roughly 15 μM. The solution was loaded in a $10 \times 10 \times 2.5$ mm^3 PMMA cuvette. After injection of the sample, which we will refer to as the bulk solvent sample, the cuvette was sealed to prevent leakage and oxygen access.

The sol-gel matrix was prepared using tetramethoxysilane (TMOS, Sigma-Aldrich Chemie GmbH, Munich, Germany) as the precursor component (Chen et al., 1986; Brinker and Scherer, 1990; Ellerby et al., 1992; Miller et al., 1996). HCl-catalyzed hydrolysis of TMOS was achieved by mixing 0.04 M HCl, millipore water and TMOS (volume ratio 1:15:67). The solution was ultrasonicated for 20 min and kept on ice before subsequent addition of the protein-cryosolvent mixture. The TMOS hydrogel and the RC containing solution (mixture of 75% glycerol and 25% buffer (10 mM Tris, 0.1% (v/v) LDAO, pH 8.0) with a final protein concentration of ≈15 μM) were mixed at a volume ratio of roughly 3:4 and kept on ice for ≈10 min. The transparent sample was filled into a $10 \times 10 \times 2.5$ mm^3 PMMA cuvette that was also used for the measurements on RCs in bulk solvent. The cuvettes were carefully sealed to prevent evaporation of water and suppress further aging. ET kinetics data were found to be identical at the beginning and end of the investigation, implying that the properties of the sol-gel matrix within the cuvette remained constant during the experiments. The described encapsulation procedure yields a hydrogel with a silica network with pore diameters of <100 Å, in which the RC proteins are embedded (Brinker and Scherer, 1990; Ellerby et al., 1992; Livage et al., 2001).

Time-resolved spectroscopy

The cuvette containing the sample was mounted in a copper sample holder which was attached to the cold finger of a closed-cycle helium refrigerator

(model 22, CTI Cryogenics, Mansfield, MA). A digital temperature controller (model 330, Lakeshore Cryotronics, Westerville, OH) was used to adjust the temperature. Light-induced electron transfer was initiated in the samples by a 6-ns (full width at half maximum) pulse (532 nm, 180 mJ) from a frequency doubled, Q-switched Nd:YAG laser (model NY 61, Continuum, Santa Clara, CA). To measure optical absorbance changes in the Soret region of the bacteriochlorophyll molecules, light from a tungsten lamp (model A 1010, PTI, Brunswick, NJ) was passed through a monochromator set at 436 nm, the sample, and a second monochromator onto a photomultiplier tube (model R5600U, Hamamatsu, Middlesex, NJ). The photocurrent was converted into a voltage, amplified and recorded with a digital storage oscilloscope from 10 ns to 50 μs (model TDS 520, Tektronix, Wilsonville, OR) and a home-made logarithmic time-base digitizer (Wondertoy II) from 2 μs to 100 s.

For light-adaptation of the RCs, light from a 250-W tungsten lamp (Oriel, Stratford, CT) was passed through a heat filter and a long pass filter (RG645, Schott GmbH, Mainz, Germany). From the signal amplitudes of transient ET kinetics of RCs cooled in the dark from 280 to 80 K, recorded both under continuous illumination and in the dark, the excitation rate, k_L, of the illumination setup can be determined (McMahon et al., 1998; van Brederode, 1999), yielding $k_L \approx 250\ s^{-1}$. With an average recombination rate of $\approx 10\ s^{-1}$ for RCs at room temperature, this implies that $\approx$95% of the RCs were trapped in the charge-separated state during cooling of the sample. To obtain ensembles with different illumination histories, light was switched on at specific temperatures T_L during cooling from 280 to 10 K. After reaching the lowest temperature (10 K), the sample was warmed in the dark at a constant ramp rate of 4.6 mK/s for both dark- and light-adapted samples. ET kinetics after flash excitation were measured every 5 K between 10 and 300 K after $\approx$3 min equilibration time at each temperature. At least five transients were averaged at each temperature, with an equilibration time of $\approx$1 min.

Numerical computations

Numerical computation of Franck-Condon (*FC*) factors according to Eq. 42 (see Appendix) was implemented on a SUN UltraSPARC-III architecture available at the computer facility of the University of Ulm, using library functions of the NAG C library (Mark 6, NAG Ltd., Oxford, UK). In our previous work, the spectral density of phonons involved in the ET reaction was truncated at 400 cm^{-1} to simplify the *FC* calculation (McMahon et al., 1998). In the new algorithm, we have shifted the cutoff frequency to 3400 cm^{-1}, which is the upper limit of vibrational modes occurring in proteins. The *FC* calculations were typically performed with a resolution in redox energy and reorganization energy of 20 meV, covering the temperature range from 0 to 305 K at a spacing of 5 K. For spectral densities with a substantial high frequency component, the resolution in redox energy was increased to $\Delta\varepsilon = 1$ meV. *FC* factors within two discrete points of evaluation were obtained via cubic spline interpolation on a logarithmic *FC* scale. All other data analysis was performed on PC workstations using the PV-WAVE package (Visual Numerics, Boulder, CO).

Experimental results and qualitative discussion

To reliably examine the influence of the sol-gel matrix on the ET properties of the protein, we have performed experiments with bulk solvent and TMOS-encapsulated RCs in parallel, using protein from the same strain and preparation. Fig. 2 shows $P^+Q_A^- \rightarrow PQ_A$ charge recombination kinetics of RCs dissolved in glycerol/buffer solution (*closed symbols*) and RCs encapsulated in a sol-gel matrix (*open symbols*) at 60, 170, and 300 K. For both dark-cooled RCs (Fig. 2 *A*) and RCs cooled under illumination from 280 K (Fig. 2 *B*), charge recombination in the TMOS sample is a factor of $\approx$2 slower than in solution. All kinetic traces are nonexponential except the solution data near 300 K.

A phenomenological, model-independent analysis of the ET kinetics provides insight into the subtle differences between both samples. For that

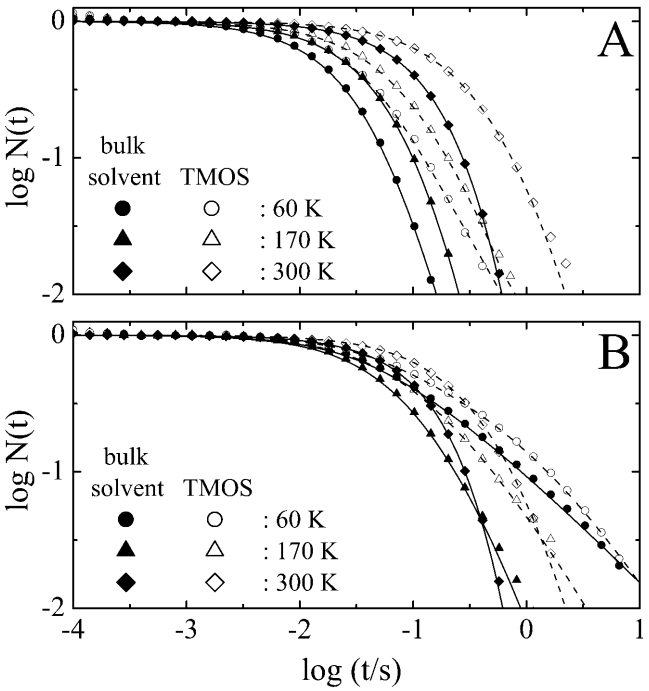

FIGURE 2 Charge recombination kinetics of RCs in a 75%/25% (v/v) glycerol/buffer mixture (*closed symbols*) and embedded in TMOS (*open symbols*) at 60 K (*circles*), 170 K (*triangles*), and 300 K (*diamonds*). (*A*) Cooled in the dark, and (*B*) cooled under illumination from 280 K. Lines represent fits according to the model described in Modeling and Quantitative Analysis.

purpose, we describe the survival probability of the charge-separated state, $N(t)$, with a distribution of rate coefficients, $f(\log k)$,

$$N(t) = \int f(\log k)\exp[-kt]d\log k. \quad (2)$$

A numerical Laplace inversion of Eq. 2 using the maximum entropy method (MEM) yields the distribution of rate coefficients (Steinbach et al., 1992). They are depicted in Fig. 3 as contour plots for RCs in bulk solvent (*left column*) and TMOS-encapsulated RCs (*right column*), cooled in the dark (*top row*), and under illumination from 280 K (*bottom row*). To illustrate the differences between samples and their illumination histories, the same scale was applied to all four maps.

To afford a more quantitative comparison, the rate distributions $f(\log k)$ in Fig. 3 can be characterized by a logarithmically averaged rate,

$$\log k_{ET} = \int f(\log k)\log k\, d\log k, \quad (3)$$

and the standard deviation σ_{ET} to quantify the width of the distribution,

$$\sigma_{ET} = \left(\int f(\log k)(\log k - \log k_{ET})^2 d\log k\right)^{1/2}. \quad (4)$$

In Fig. 4 we plot these two quantities for the distributions shown in Fig. 3. We have also included data from an experiment in which the illumination during cooling was switched on at 180 K.

The sample in cryosolvent exhibits the same overall features that were observed in earlier experiments on carotenoid-deficient RCs (McMahon et al., 1998). ET kinetics of dark-cooled RCs speed up by a factor of $\approx$6 upon cooling from room temperature to 10 K, from $k_{ET} \approx 8.7$ to 50 s^{-1}. A pronounced step occurs in the temperature range between 160 and 200 K, as seen in Figs. 3 *A* and 4 *A*. A slight increase of the average rate coefficient

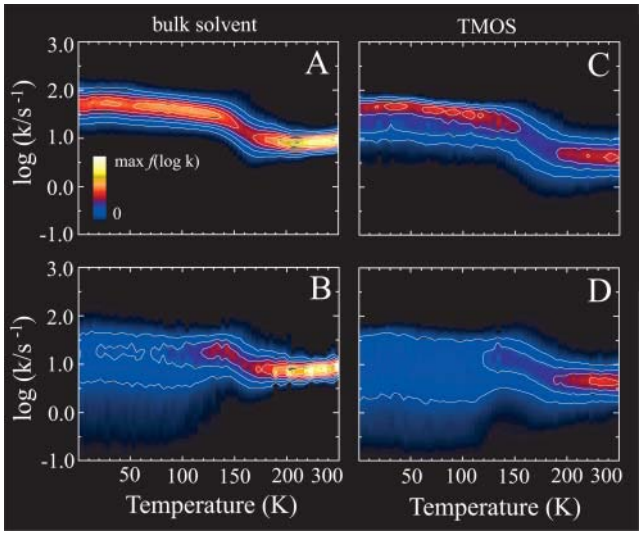

FIGURE 3 Contour plots of the distributions of rate coefficients, $f(\log k)$, between 10 and 300 K with linear spacing of contour lines. All plots were scaled identically to illustrate the differences between samples and illumination histories. (*A*) Bulk solvent, cooled in the dark; (*B*) bulk solvent, cooled under illumination from 280 K; (*C*) TMOS hydrogel matrix, cooled in the dark; and (*D*) TMOS hydrogel matrix, cooled under illumination from 280 K.

from 7.5 to 8.7 s^{-1} is observed between at 250 and 300 K. At 10 K, the width of the distribution is $\sigma_{ET} = 0.2$. At ~200 K, σ_{ET} exhibits a broad maximum extending over a temperature interval of 50 K. The distribution narrows toward 300 K, with $\sigma_{ET} = 0.1$ as obtained from the MEM. This width, however, represents exponential (nondistributed) behavior within the noise statistics of our data. A completely different behavior is observed after cooling the cryosolvent sample from 280 K under illumination. At 10 K, k_{ET} is about the same as at 300 K, and upon warming, an excursion toward faster rates is evident, extending over temperatures ranging from 120 to 200 K. Above 250 K, the k_{ET} data essentially merge with those of the dark-adapted preparation. The width of the rate distribution is about threefold larger at 10 K as compared with the dark-cooled sample. Concomitant with the excursion of k_{ET} above 120 K, the width of the distribution narrows and merges with that of the dark-cooled sample above 200 K.

A dip in the rate coefficients occurs universally below 50 K. Its magnitude depends on the illumination conditions and thus reflects light-induced conformational changes. This effect is likely related to observations made by spectral hole burning and will not be considered here (Ganago et al., 1991; Reddy et al., 1992).

The temperature-dependent features in the data (above 50 K) can be understood with the schematic in Fig. 5. Cooling in the dark arrests the dark-adapted state with fast recombination kinetics at 10 K. From ~50 to 170 K, the protein ensemble is frozen-in on the timescale of charge separation (Fig. 5, *A* and *B*), and the slowing arises solely from the intrinsic temperature dependence of the ET reaction (vide infra). The steep drop from 170 to 200 K and the subsequent step up to 250 K are caused by the protein ensemble relaxing on the $P^+Q_A^-$ energy surface during the (millisecond) lifetime of the charge-separated state (Fig. 5, *C* and *D*). The quantitative analysis shows that this leads to a decrease of the energy gap and concomitant slowing of the ET rate. This dynamic model is further supported by the observation that the rate distribution broadens over the temperature interval in which charge

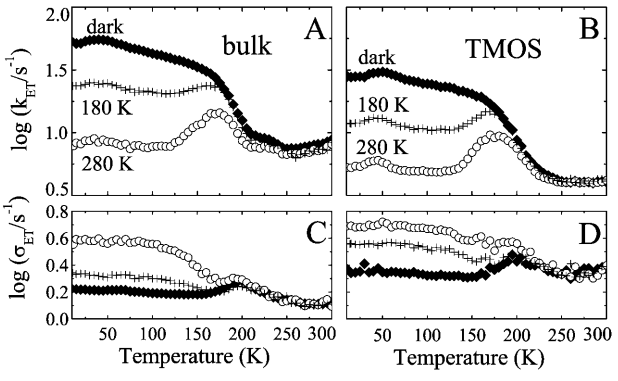

FIGURE 4 Temperature dependence of parameters characterizing the ET rate distributions. Logarithmically averaged charge recombination rate, log k_{ET}, (*A*) for RCs in bulk solvent and (*B*) for RCs immobilized in TMOS matrix. Width σ_{ET} of the rate distributions, (*C*) for RCs in bulk solvent, and (*D*) for RCs encapsulated in TMOS. Samples were either cooled in the dark (*diamonds*) or under illumination from 180 K (*crosses*) and 280 K (*open circles*).

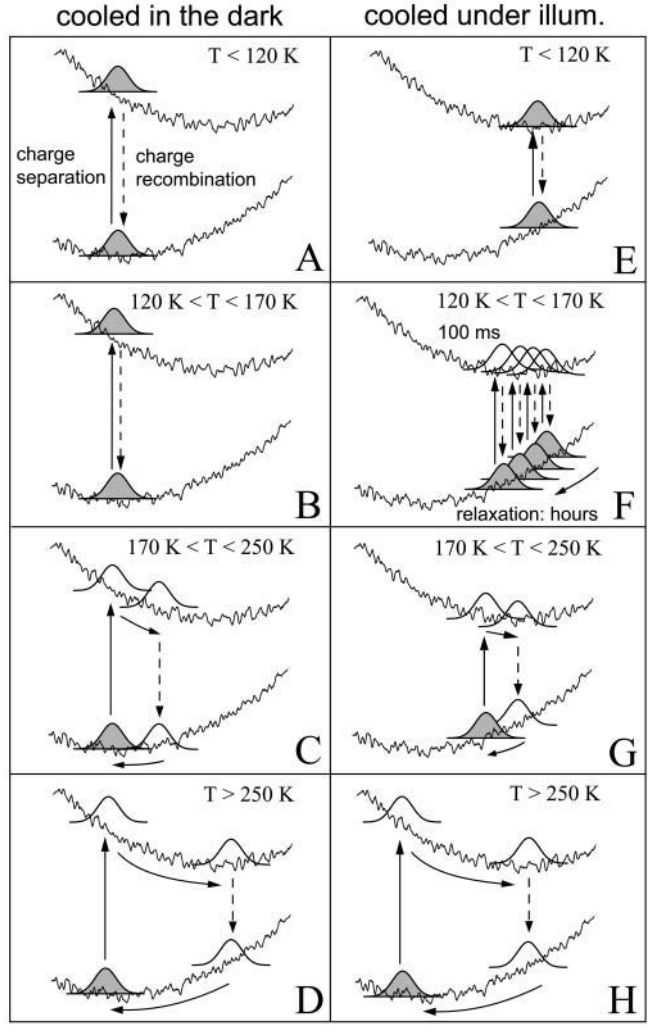

FIGURE 5 Evolution of the protein ensembles in different temperature ranges due to relaxation on the energy surfaces associated with the neutral and charge-separated states, for samples cooled in the dark (*left, A–D*) or under illumination from room temperature (*right, E–H*). A detailed description is given in the text.

recombination occurs while the protein ensemble is diffusing downhill on the excited state surface. Above 250 K, relaxation is complete within the lifetime of the charge-separated state so that recombination occurs from around the minimum of the $P^+Q_A^-$ energy surface at $q = 1$.

Cooling under illumination arrests the ensemble in the light-adapted state. At 10 K, k_{ET} is almost identical to the value at room temperature, reflecting the smaller energy gap at $q = 1$ (Fig. 5 *E*). As the temperature is slowly increased, protein dynamics is initially frozen in. But then, at ≈120 K, an increase of k_{ET} signals that the ensemble begins to slowly develop toward $q = 0$. It migrates over hours on the lower surface (Fig. 5 *F*), and the relaxation dynamics can be observed over h instead of ms as in the dark-cooled preparation. A maximum occurs at 175 K. At this point, relaxations on the upper surface become important again, leading to a subsequent decay toward 200 K (Fig. 5 *G*). Above 250 K, the RCs relax completely on the upper energy surface within the lifetime of the charge-separated state (Fig. 5 *H*). The extent of relaxation can be quantified by the gap between the dark- and light-cooled k_{ET} curves. The temperature dependence of the width σ_{ET} also supports this dynamic scenario. It decreases markedly above 120 K and merges with that of the dark-adapted sample near 200 K. Fig. 4 also includes data measured after switching light on at 180 instead of 280 K during cooling. At 180 K, motions on the rugged energy surface are substantially slowed and partially arrested so that the protein ensemble becomes trapped on part of the way between $q = 0$ and 1. Consequently, data from this experiment interpolate between the other two data sets.

RCs immobilized in TMOS hydrogels exhibit qualitatively the same behavior as solvent samples. The temperature dependence of the rate distributions is similar, with the step in k_{ET} of the dark-cooled sample between 160 and 200 K and the excursion of k_{ET} of the light-cooled sample in the intermediate temperature range. It is evident that protein motions solvating the charges are not suppressed in the hydrogel. However, there are also significant differences. For both dark- and light-cooled samples, recombination is slower by a factor of ≈2 over the entire temperature range in RCs in a sol-gel matrix than in cryosolvent. The overall width σ_{ET} is larger than that of the bulk sample (Fig. 4, *C* and *D*), and the kinetics remain clearly nonexponential even at room temperature. A pronounced difference between solution and hydrogel is apparent from comparing k_{ET} above 200 K. Whereas the solvent sample exhibits a discrete step in k_{ET} between 200 and 250 K, the TMOS sample shows a smooth and continuous decay, and k_{ET} remains constant above 250 K. With a detailed analysis of the temperature dependence of ET in a solution sample we had shown earlier that the step between 200 and 250 K is associated with the presence of global conformational motions (McMahon et al., 1998). The lack of this step suggests, therefore, that global fluctuations between markedly different conformations are suppressed in the sol-gel matrix. This conclusion is also in agreement with the observed widths of the rate distributions. From 200 to 250 K, the rate distribution of the solution sample collapses to essentially exponential behavior, indicating that even the slowest global fluctuations affecting ET become faster than k_{ET}. By contrast, the rate distributions of TMOS encapsulated RCs narrow only slightly and stay constant above 250 K. The nonexponential kinetics even at 300 K clearly show that the RCs entrapped in the gel are structurally heterogeneous. While local dynamics is possible in the gel, fluctuations among globally distinct conformations are arrested on the ET timescale.

Finally, there is another significant difference between bulk solvent and encapsulated RC samples. When cooling under illumination from 280 K, the signal amplitude of the solvent sample at 10 K is only 20% of that at 300 K, but 50% for the TMOS sample. This effect is completely reversible, however, and recovery of the signal amplitudes occurs at ~250 K in both samples.

From this phenomenological discussion of the $P^+Q_A^- \rightarrow PQ_A$ kinetics, two main questions arise. First, why are the charge recombination kinetics in RCs that are immobilized in a silica gel markedly slower than in bulk solvent? And second, how are relaxations and fluctuations among different conformational substates influenced by the hydrogel matrix? To address these questions, we present a quantitative analysis of the ET kinetics based on a quantum-mechanical model that allows us to map the distribution of rate coefficients onto a distribution of a physical parameter, the energy gap ε.

MODELING AND QUANTITATIVE ANALYSIS

Microscopic ET rates

In his pioneering work on electron transfer reactions in solution, Marcus derived the well-known formula for the ET rate coefficient (Marcus, 1964; Marcus and Sutin, 1985),

$$k(\varepsilon, \lambda; T) = \frac{2\pi}{\hbar} V^2 \frac{1}{\sqrt{4\pi\lambda k_B T}} \exp\left[-\frac{(\varepsilon - \lambda)^2}{4\lambda k_B T}\right], \quad (5)$$

where V is the electronic coupling between reactant and product state, ε and λ denote the free energy difference between the two redox states and the reorganization energy, respectively, k_B is Boltzmann's constant, $\hbar$ Planck's constant divided by 2π, and T is the absolute temperature. This expression has been applied successfully to a variety of redox systems in nonbiological as well as in biological systems (Marcus and Sutin, 1985; Gray and Malmström, 1989; Moser et al., 1992).

Marcus's rate law is the classical version of the general expression for nonadiabatic ET transfer, in which the microscopic rate coefficient is given by Fermi's golden rule, using the Condon approximation (Levich and Doganadze, 1959; Jortner, 1976),

$$k(T) = \frac{2\pi}{\hbar} V^2 FC, \quad (6)$$

with the thermally averaged *FC* factor, which is a measure for the overlap of the nuclear wavefunctions between the reactant and product state. Comparison with Eq. 5 shows that, in the classical case, *FC* depends on the redox energy ε, the reorganization energy λ, and the temperature T.

However, Marcus's expression is only applicable at temperatures sufficiently high that equipartition holds for *all* vibrational modes coupled to the ET reaction. In biological ET, however, quantum effects are important even at room temperature. Therefore, we use the spin-boson model to evaluate the *FC* factors. This model provides a quantum-mechanical description of ET coupled to a continuous spectrum of harmonic oscillators, which is characterized by its spectral density $J(\omega)$ (Garg et al., 1985; Onuchic et al., 1986; Warshel and Hwang, 1986; Leggett et al., 1987; Warshel et al., 1989; Xu and Schulten, 1992; Xu and Schulten, 1994). The temperature and free energy dependence of the *FC* factor is given in terms of the spectral density $J(\omega)$, which is related to the reorganization energy λ by (Xu and Schulten, 1994)

$$\lambda = \frac{1}{\pi} \int \frac{J(\omega)}{\omega} d\omega. \quad (7)$$

We model $J(\omega)/\omega$ as a sum of a Lorentzian, centered at $\omega = 0$ and characterized by its linewidth ω_s, and a few Gaussians centered at higher frequencies $\omega_i > 0\ \mathrm{cm}^{-1}$ with variance σ_i^2,

$$\frac{J(\omega)}{\omega} = \frac{S_s}{1 + \frac{\omega^2}{\omega_s^2}} + \sum_i S_i \exp\left[-\frac{(\omega - \omega_i)^2}{2\sigma_i^2}\right], \qquad (8)$$

where S_s and S_i denote the coupling strengths. A more elaborate description of the spin-boson model will be given in the Appendix.

In our analysis of the charge recombination kinetics, we describe the structural heterogeneity of the protein ensemble by a distribution of energy gaps, $g(\varepsilon)$, which depends on temperature and the illumination protocol applied before the experiment. The energy gap distribution is related to the distribution of the rate coefficients, $f(\log k)$, by

$$g(\varepsilon)d\varepsilon = f(\log k)d\log k. \qquad (9)$$

In contrast to the free energy gap ε, the spectral density $J(\omega)$ (and thus the reorganization energy λ) is taken to be temperature independent. Furthermore, the electronic coupling matrix element V is assumed to depend logarithmically on the free energy gap ε. This is modeled by introducing a pivot point ε_0 and a stretch factor γ,

$$\log V = \log V_0 + \gamma(\varepsilon - \varepsilon_0), \qquad (10)$$

with temperature-independent parameters V_0, γ, and ε_0. The assumptions underlying Eq. 10 are discussed in detail in McMahon et al. (1998). This approach allows us to recast Eq. 2 in terms of a single physical parameter, the energy gap ε:

$$N(t) = \int g(\varepsilon)\exp[-k(\varepsilon)t]d\varepsilon. \qquad (11)$$

Determination of temperature-independent ET parameters

From the classical Marcus formula (Eq. 5), which is equivalent to the spin boson model in the high temperature limit (Xu and Schulten, 1992), it is obvious that various combinations of the parameters ε, V, and λ characterizing the redox system yield the same rate coefficient at a particular temperature. Whereas the redox energy ε can be determined by experimental means, for instance redox titration (Moss et al., 1991; Lin et al., 1994; Paschenko et al., 2001), delayed fluorescence measurements (Arata and Parson, 1981), or direct voltammetry (Kong et al., 1998), the reorganization energy λ is not directly accessible to experiment (Sharp, 1998). To model charge recombination from the primary quinone Q_A in RCs of *Rb. sphaeroides*, several authors reported varying combinations of V and λ, all yielding convenient fits of the ET kinetics (Gunner et al., 1986; Ortega et al., 1996; McMahon et al., 1998; Schmid and Labahn, 2000). Therefore, a self-consistent method is necessary to determine these parameters. In our experimental approach, we measure the charge recombination kinetics as a function of both temperature and illumination protocol. This allows us to extract temperature-independent parameters from the intrinsic temperature dependence of the microscopic ET rates. Moreover, we can also quantify the effects of protein motions on the ET reaction.

To determine the temperature-independent parameters, λ, V_0, γ, and ε_0, we exploit a peculiarity of activationless ET. A calculation of rate coefficients $k(\varepsilon, T)$ for fixed reorganization energy λ (Fig. 6) shows, that, depending on the redox energy ε, the ET kinetics either speed up or slow down with increasing temperature. Both regions are separated by a region with essentially temperature-independent rate coefficients. In the following, we refer to this point of minimal temperature dependence, $\{\varepsilon_{iso}, k_{iso}\}$, as the isokinetic point. This behavior can be examined directly by comparing subsequent kinetics traces $N(t, T)$ with increasing temperature T. The dispersion of the ET kinetics with respect to temperature can be quantified by calculating the sum over all pair differences,

$$\Delta_p(t) = \frac{2}{n_T(n_T - 1)} \sum_{\substack{i,j=1 \\ T_i < T_j}}^{n_T} \{N(t, T_i) - N(t, T_j)\}, \qquad (12)$$

where n_T denotes the total number of kinetic traces. Fig. 7 *A* shows $\Delta_p(t)$ for dark-cooled (*filled triangles*) and light-

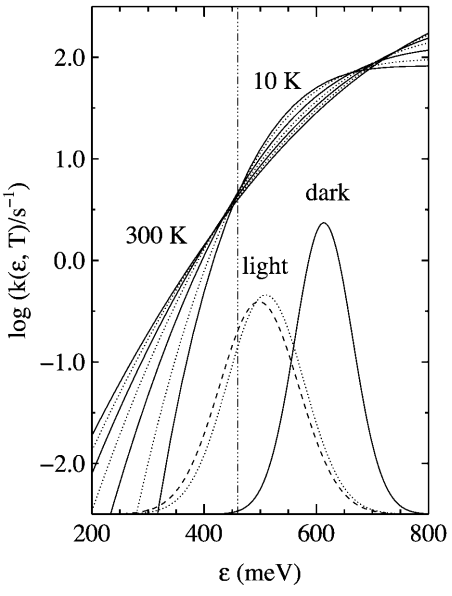

FIGURE 6 Microscopic rate coefficients $k(\varepsilon, T)$ as a function of ε, calculated with the spin boson model at 10, 50, 100, 150, 200, 250, and 300 K (alternating *solid* and *dotted lines*). Also shown are three Gaussian $g(\varepsilon)$ distributions, the one that was used to optimize the temperature-independent ET parameters (*dotted line*), and the fit results for the dark-cooled sample (60 K, *solid line*) and a sample cooled under illumination from 280 K (60 K, *dashed line*). For details, see the text.

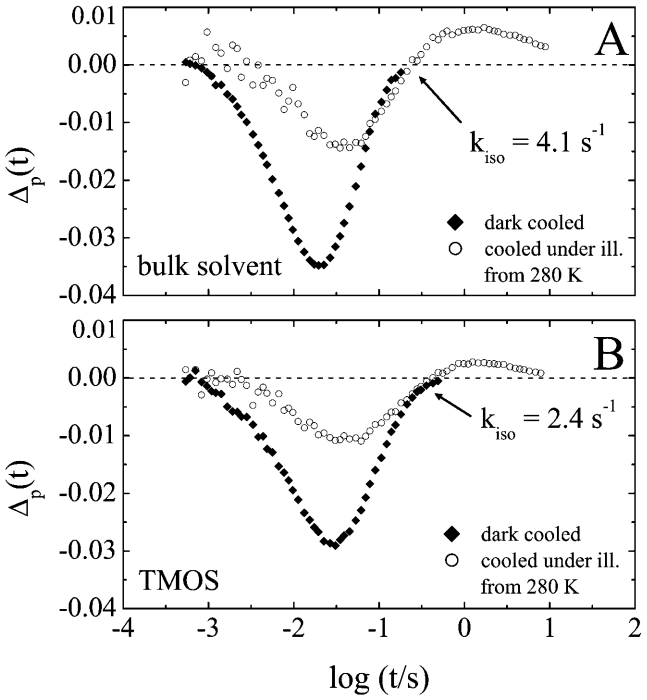

FIGURE 7 Sum of pair differences, $\Delta_p(t)$, from kinetic traces measured between 60 and 120 K. (*A*) Bulk solvent RCs. (*B*) RCs embedded in TMOS: dark-cooled (*diamonds*), sample cooled under illumination from 280 K (*open circles*); and isokinetic points (*arrows*).

cooled (*open circles*) RCs in cryosolvent, calculated for temperatures between 60 and 120 K (5 K intervals). Whereas the kinetics of the dark-cooled sample slow down continuously with increasing temperature, as inferred from the sign of $\Delta_p(t)$, cooling under illumination leads to a more complex behavior: for $t < 0.24$ s, the kinetics speed up with temperature; for $t > 0.24$ s, the opposite is observed. Thus, $t_{iso} = 0.24$ s indicates an isokinetic point. From the sign of $\Delta_p(t)$ and the isokinetic point, the location of the distributions of redox energies, $g(\varepsilon)$, can thus be estimated for both samples: the majority of the distribution characterizing dark-cooled RCs in cryosolvent is located at redox energies larger than ε_{iso}; for bulk RCs cooled under illumination, the distribution is centered near the isokinetic point ε_{iso}.

Along with the reorganization energy λ, the electronic coupling matrix element V_0 and the factors relating ε and V_0, γ, and ε_0, have to be determined. Besides the isokinetic point k_{iso}, we take advantage of two additional features of charge recombination kinetics. First, we assume that the microscopic rate coefficient for nonadiabatic ET, k_{RT}, is well approximated by the Marcus expression, Eq. 5, at the highest temperatures studied. With the redox energy at room temperature (300 K), ε_{RT}, determined by independent experimental means (Arata and Parson, 1981; Moss et al., 1991; Lin et al., 1994; Paschenko et al., 2001), the interdependence of the electronic coupling, V, and the reorganization energy, λ, is given by

$$V(\lambda) = \left(\frac{\hbar\sqrt{4\pi\lambda k_B T}}{2\pi} k_{RT} \exp\left[\frac{(\varepsilon_{RT} - \lambda)^2}{4\lambda k_B T}\right]\right)^{1/2}, \quad (13)$$

where the rate coefficient at room temperature, k_{RT}, is taken from the experimental data. Second, we compare the maximum rate obtained for dark-cooled samples, k_{max}, and the rate at the isokinetic point, k_{iso}. We define k_{max} heuristically such that 5% of the distribution covers still faster rates,

$$\int_{\log k_{max}}^{\infty} d\log k f(\log k) = 0.05, \quad (14)$$

with the rate distribution $f(\log k)$ as obtained from a MEM analysis of the charge recombination kinetics of dark cooled RCs. From the spin-boson model, the ratio $\varrho = k_{max}/k_{iso}$ can be calculated as a function of γ and reorganization energy λ for fixed pivot points ε_0, whereas different reorganization energies are achieved by an appropriate, concurrent scaling of the coupling constants S_S and S_i in Eq. 8. At fixed ϱ, λ can be computed numerically as a function of γ. Both relations lead to a unique interdependence of the temperature-independent parameters λ, V, and γ, which is illustrated for RCs in bulk solvent in Fig. 8.

Conformational motions can be neglected below 120 K. Therefore, the protein ensemble cooled under illumination from room temperature remains in the light-adapted conformation, which is characterized by a distribution of energies gaps, $g_L(\varepsilon)$, centered at the room temperature value ε_{RT}. For simplicity, we assume a Gaussian shape,

$$g_L(\varepsilon) = \frac{1}{\sqrt{2\pi}\sigma_L} \exp\left[-\frac{(\varepsilon - \varepsilon_{RT})^2}{2\sigma_L^2}\right]. \quad (15)$$

With the distribution of energy gaps, $g_L(\varepsilon)$, kept fixed between 60 and 120 K and the interdependence of λ, V_0, and γ as shown in Fig. 8, a parameter triple λ, V_0, and γ can be iteratively determined that reproduces the observed isokinetic point. Within the optimization procedure, a variation of the pivot point ε_0 is reflected in a change of the electronic coupling matrix element V_0, whereas both the reorganization energy λ and the scaling factor of the interdependence of the electronic coupling matrix element V_0 and redox energy ε, γ, remain unaffected. Therefore, we chose $\varepsilon_0 = \varepsilon_{RT}$ in our calculations. The rate at the isokinetic point also depends on the width σ_L of $g_L(\varepsilon)$. Thus, we use the width of the distribution of rate coefficients, σ_{ET}, obtained from the MEM analysis of the ET kinetics (Eq. 4), as an additional criterion in the parameter determination.

As a final step in the determination of the temperature-independent parameters, an appropriate shape of the spectral density $J(\omega)$ has to be selected. High frequency modes with short lifetimes give rise to a flattening of the $k(\varepsilon, T)$ curves. The dispersion of the microscopic rate coefficients with respect to temperature, $d\log k/dT$, at fixed redox energy ε and reorganization energy λ is reflected in the steepness

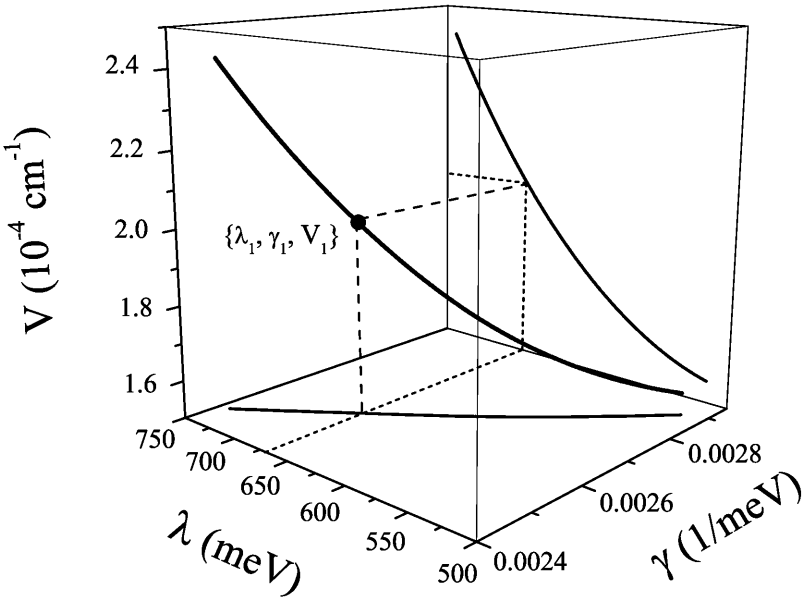

FIGURE 8 Interdependence of reorganization energy, λ; electronic coupling matrix element, V; and parameter γ (Eq. 10) as obtained from a rearrangement of the Marcus expression Eq. 13 (projection onto the V-λ plane) and the ratio ϱ between the fastest rate, k_{max}, and the rate at the isokinetic point, k_{iso} (projection onto the λ-γ plane). The calculation was performed for bulk solvent RCs using the parameters compiled in Table 1.

of the sum of pair differences, $\Delta_p(t)$. The larger $|d \log k(\varepsilon, T)/dT|$, the more pronounced are the differences observed between subsequent kinetic traces $N(t, T_i)$ and $N(t, T_j)$ at a fixed distribution of redox energies, and vice versa. This is illustrated in Fig. 9 *A*, where the sum of pair differences $\Delta_p(t)$ is shown for different parameterizations of the spectral density (*inset*, Fig. 9 *A*) after iterative determination of the temperature-independent ET parameters. The open squares represent the experimental results obtained from bulk RCs cooled under illumination from 280 K. As a quantitative criterion for the choice of parameters governing the spectral density $J(\omega)$, we use the residuals $R(t)$ of the sum of pair differences, shown in Fig. 9 *B*. They are defined as

$$R(t) = \frac{\Delta_p^{opt}(t) - \Delta_p^{exp}(t)}{\sigma_\Delta(t)}. \quad (16)$$

Here, $\Delta_p^{opt}(t)$ is obtained from the parameter optimization, and $\Delta_p^{exp}(t)$ denotes the sum of pair differences calculated from the experimental data. The standard deviations $\sigma_\Delta(t)$ have been determined from the statistics of each kinetic trace $N(t, T)$. Minimization of the residuals $R(t)$ yields a suitable parameterization of the spectral density. Note that we have not applied any fitting routine to analyze each individual kinetic trace so far; the optimization algorithm, nevertheless, reproduces the sum of pair differences very well.

Fig. 6 shows $k(\varepsilon, T)$ curves obtained for bulk solvent RCs from the optimization algorithm described above, together with the static distributions of energy gaps of the light-adapted and dark-adapted conformations. The temperature-independent ET parameters are summarized in Table 1.

The identical parameter optimization procedure has also been applied to RCs embedded in the TMOS matrix. The sums of pair differences $\Delta_p(t)$ in Fig. 7 *B* exhibit a similar

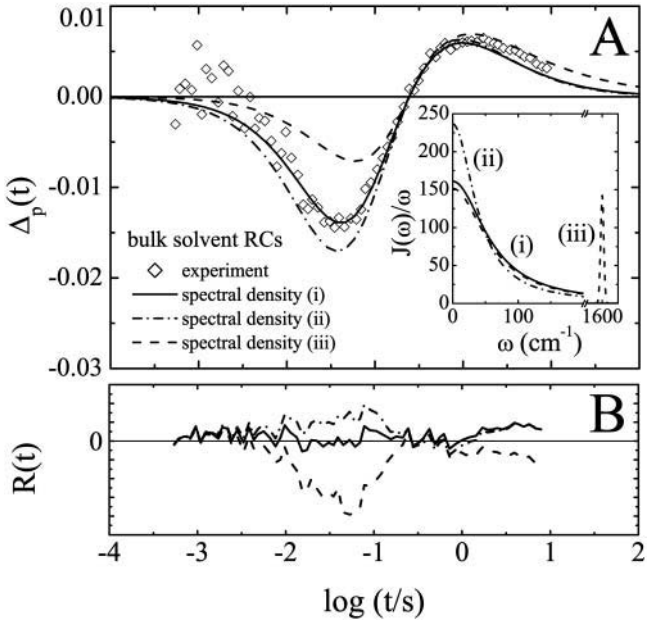

FIGURE 9 Dependence of pair differences, $\Delta_p(t)$, on the shape of the spectral density $J(\omega)$. (*A*) $\Delta_p(t)$ from experiments on bulk RCs cooled under illumination from 280 K (*diamonds*) and from calculations using the spectral densities plotted in the inset as $J(\omega)/\omega$ in units of $\hbar$ (shown with *corresponding line styles*). For (*iii*), a 1600-cm^{-1} mode contributes 20% to the total reorganization energy. (*B*) Residuals $R(t)$ of the sum of pair differences shown in *B*.

TABLE 1 Temperature-independent parameters of the electron transfer model

Sample	ϱ	k_{iso} [s^{-1}]	k_{RT} [s^{-1}]	ε_{RT} [meV]	λ [meV]	V_0 [10^{-4} cm^{-1}]	γ [1/meV]
Bulk solvent	34.1	4.1	8.7	510	593	1.70	0.0027
TMOS	33.3	2.4	4.0	510	600	1.17	0.0027

The pivot point ε_0 was fixed at 510 meV for both bulk solvent RCs and RCs encapsulated in TMOS.

pattern as their bulk solvent counterparts, suggesting that the analysis applied to bulk solvent RCs should also be valid for TMOS encapsulated RCs. The parameters, which are included in Table 1, are overall similar to those of RCs in bulk solvent. Two differences are noteworthy. The electronic coupling matrix element V_0 is reduced compared to bulk solvent. This difference directly affects the position of the isokinetic point, which can be read off from Fig. 7 *B* as $t_{iso} = 0.42$ s for TMOS-encapsulated RCs instead of $t_{iso} = 0.24$ s obtained for bulk RCs. Moreover, the amplitude of $\Delta_p(t)$ is smaller for TMOS-encapsulated RCs, which can be traced back to a broadening of the distribution of energy gaps. Indeed, the width of the Gaussian characterizing the freeze-trapped, light-adapted protein ensemble is ≈15 meV larger compared to the value obtained for bulk solvent RCs.

Fit results

After determination of the temperature-independent parameters of the model, the charge recombination kinetics were fitted individually by applying Eq. 11, using a nonlinear least-squares Levenberg-Marquardt algorithm. In the simplest fashion, one can parameterize the distribution of redox energies, $g(\varepsilon)$, by a single Gaussian. However, deviations from a symmetric distribution of energy gaps can be envisioned from different topographies of the potential surfaces representing the charge-separated ($P^+Q_A^-$) and charge recombined state (PQ_A), respectively, as depicted in Fig. 1. Flash-induced charge recombination kinetics probe a distribution of redox energies, $g(\varepsilon)$, rather than the initial distribution of conformations, $p(q, T = T_0)$. The mapping is given by

$$p(q, T = T_0)dq = g(\varepsilon)d\varepsilon, \tag{17}$$

where the redox energy ε is a function of the conformational coordinate q (Fig. 1).

Only for harmonic potentials with the same first derivative, the mapping is linear, resulting in a conserved shape of $p(q, T = T_0)$. In general, this may not be the case. If we assume the initial distribution of conformations to be Gaussian, as expected for evenly distributed random variables, the distribution of redox energies observed in charge recombination kinetics appears as an asymmetric distribution. To account for both symmetric and asymmetric distributions of redox energies, charge recombination kinetics were fitted with a single Gaussian or a sum of two Gaussians,

$$g(\varepsilon) = \nu\frac{1}{\sqrt{2\pi}\sigma_1}\exp\left[-\frac{(\varepsilon-\varepsilon_1)^2}{2\sigma_1^2}\right] + (1-\nu)\frac{1}{\sqrt{2\pi}\sigma_2}\exp\left[-\frac{(\varepsilon-\varepsilon_2)^2}{2\sigma_2^2}\right]. \tag{18}$$

As with $f(\log k)$, we characterize the $g(\varepsilon)$ distribution by its first moment, $\langle\varepsilon\rangle$, and its second moment, σ_ε, given by

$$\langle\varepsilon\rangle = \int_0^\infty \varepsilon g(\varepsilon)d\varepsilon \tag{19}$$

and

$$\sigma_\varepsilon = \left(\int_0^\infty g(\varepsilon)(\varepsilon - \langle\varepsilon\rangle)^2 d\varepsilon\right)^{1/2}. \tag{20}$$

In the fit, the peak and width parameters of the $g(\varepsilon)$ were varied. For bulk solvent RCs, a single Gaussian $g(\varepsilon)$ distribution described the charge recombination kinetics of both dark-cooled RCs and RCs cooled under illumination from different temperatures appropriately throughout the whole temperature range. Only between 120 and 180 K, the fit quality was slightly reduced. The distributions at 60 K for dark cooled RCs and RCs cooled under illumination from 280 K are depicted as solid and dotted lines in Fig. 6, respectively. Also shown is the static $g(\varepsilon)$ distribution that was used in the parameter optimization (*dashed line*), showing a deviation by only 3% of the peak position from the fit result. The kinetics at 60, 170, and 300 K calculated from the fit are shown as solid lines in Fig. 2, illustrating the ability of our ET model to precisely reproduce the experimental data without introducing fit parameters beyond those mentioned above. The center positions $\langle\varepsilon\rangle$ and widths σ_ε of the Gaussians are depicted as a function of temperature between 60 and 300 K for both dark cooled samples and samples cooled under illumination in Fig. 10, *A* and *C*, respectively. They reproduce the behavior deduced from the temperature dependence of rate distributions in Fig. 4, *A* and *C*.

For the sol-gel matrix preparation, the kinetics of dark-cooled RCs and RCs cooled under illumination from 180 K were well fitted using a single Gaussian $g(\varepsilon)$. For RCs cooled under light from 280 K, the distribution was clearly asymmetric and, therefore, we used the two-Gaussian distribution. From our data we cannot identify the origin for the asymmetry present in the light-adapted ensemble. Slight distortions of the potential surfaces are conceivable, leading to a nonlinear mapping between ε and q (Eq. 17). The presence of a significant fraction that was not freeze-trapped

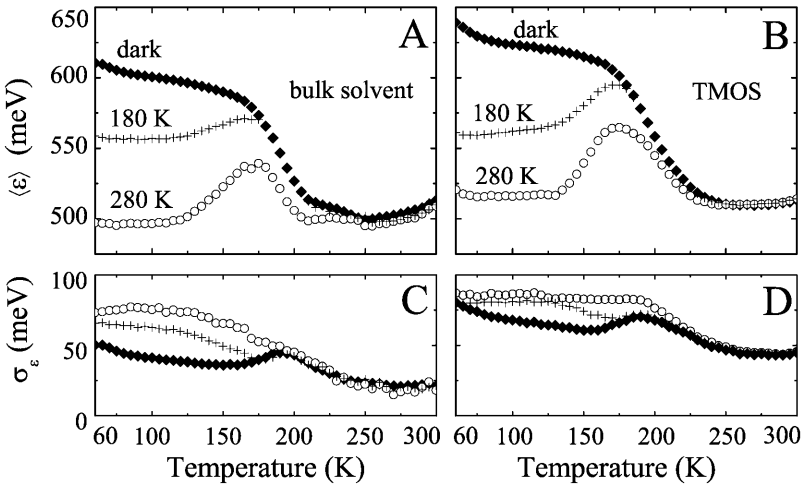

FIGURE 10 Parameters characterizing the $g(\varepsilon)$ distributions as obtained from the fit. Average energy gaps, $\langle\varepsilon\rangle$, for (*A*) bulk RCs and (*B*) TMOS encapsulated RCs cooled in the dark (*diamonds*), and under illumination from 180 K (*crosses*) and 280 K (*circles*). Widths, σ_ε, for (*C*) bulk solvent RCs and (*D*) TMOS encapsulated RCs.

in the light-adapted state due to restrictions introduced by the TMOS matrix can be excluded because of the temperature dependence of $\langle\varepsilon\rangle$ and σ_ε (Fig. 10, *B* and *D*) which tracks their bulk solvent counterpart perfectly. The individual fits are shown as dashed lines in Fig. 2, *A* and *B*. The mean energy gap $\langle\varepsilon\rangle$ of the dark-cooled TMOS encapsulated RCs between 60 and 120 K is ≈4% higher compared to the value obtained for bulk solvent RCs, indicating a slight variation of the energetics governing ET upon sol-gel encapsulation. The parameters characterizing the 60 K distributions of energy gaps for both bulk solvent and TMOS entrapped RCs are compiled in Table 2.

Following our previous work (McMahon et al., 1998), we introduce a phenomenological relaxation function $\Phi(T)$, which is defined for dark-adapted (*D*) and light-adapted (*L*) RCs as

$$\Phi_{\mathrm{D}}(T) = \frac{\langle\varepsilon_{\mathrm{D}}(T)\rangle - \langle\varepsilon_{\mathrm{D}}(T_1)\rangle}{\langle\varepsilon_{\mathrm{D}}(T_0)\rangle - \langle\varepsilon_{\mathrm{D}}(T_1)\rangle}, \tag{21}$$

and

$$\Phi_{\mathrm{L}}(T) = \frac{\langle\varepsilon_{\mathrm{D}}(T)\rangle - \langle\varepsilon_{\mathrm{L}}(T)\rangle}{\langle\varepsilon_{\mathrm{D}}(T_0)\rangle - \langle\varepsilon_{\mathrm{D}}(T_1)\rangle}, \tag{22}$$

respectively. Here, the difference $\langle\varepsilon_{\mathrm{D}}(T_0)\rangle - \langle\varepsilon_{\mathrm{D}}(T_1)\rangle$ defines the maximum relaxation amplitude of the conformational coordinate $\langle\varepsilon\rangle$, with $\varepsilon_{\mathrm{D}}(T_1)$ denoting the fully relaxed protein.

Fig. 11, *A* and *C*, shows both $\Phi_{\mathrm{D}}(T)$ and $\Phi_{\mathrm{L}}(T)$ and their derivatives with respect to T, $|d\Phi/dT|$, for bulk solvent RCs. We have restricted the relaxation functions to the temperature interval from $T_0 = 60$ K to $T_1 = 250$ K to exclude the additional complications present outside of this temperature window. The relaxation function $\Phi(T)$ shows four steps, which represent different relaxation processes activated in subsequent temperature regions. We had earlier assigned these steps to conformational fluctuations in different tiers of the hierarchy of conformational substates, CS3, CS2, CS1, and CS0, in ascending order (McMahon et al., 1998). Relaxation functions and derivatives for TMOS encapsulated RCs are depicted in Fig. 11, *B* and *D*. Although they exhibit an overall similar shape compared to their bulk solvent counterparts, there are significant differences. The onset temperatures and amplitudes of the CS2 and CS1 relaxations differ for both preparations. In the hydrogel, these motions occur at somewhat higher temperatures and are not so clearly separated. Most interesting, however, is the behavior of $\Phi(T)$ above 200 K. For the dark-cooled bulk solvent preparation, $\Phi(T)$ clearly exhibits a well-separated step with a much weaker decay from 200 to 250 K. This feature has been associated with global conformational rearrangements of the RC proteins (McMahon et al., 1998). In contrast, the corresponding relaxation function for the TMOS sample decays smoothly from 180 to 250 K.

TABLE 2 Energy gap distributions at 60 K

	Bulk solvent		TMOS	
Conformation	ε [meV]	σ_ε [meV]	ε [meV]	σ_ε [meV]
Dark-adapted	610	50	635	80
Light-adapted	497	73	520	85

DISCUSSION

Dependence of ET rates on temperature and illumination protocol

In their pioneering work, Kleinfeld and co-workers observed a drastic decrease of the average rate of $P^+Q_{\mathrm{A}}^-$ charge recombination upon cooling RCs under illumination, which was accompanied by a substantial broadening of the lifetime distribution of the charge separated state, as compared with dark-cooled RCs (Kleinfeld et al., 1984). Their initial analysis invoked a dependence of the donor-acceptor distance on the illumination history, yielding an increase of the mean distance between the special pair *P* and quinone Q_{A} by 1 Å upon cooling under illumination. On a molecular

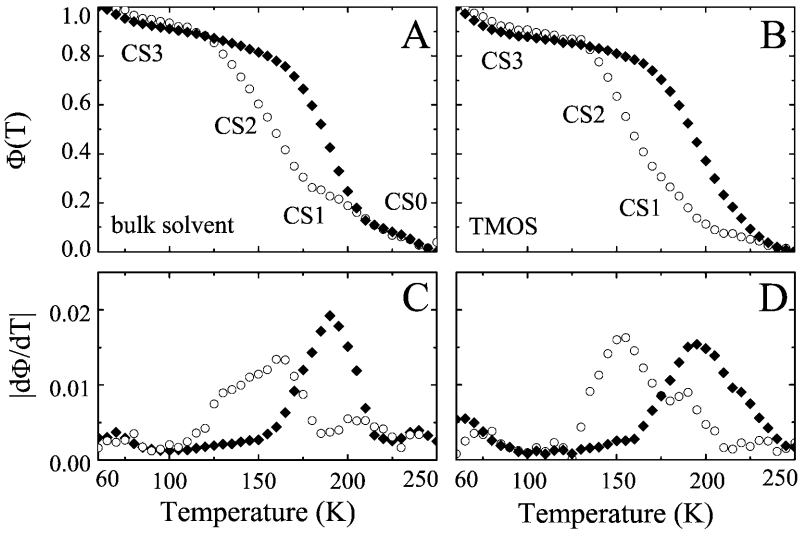

FIGURE 11 Relaxation functions, $\Phi(T)$, for dark-adapted and light-adapted RCs, as defined in Eqs. 21 and 22, and their first derivatives with respect to temperature. $\Phi_D(T)$ (*closed diamonds*) and $\Phi_L(T)$ (*open circles*) for (*A*) bulk solvent RCs and (*B*) TMOS encapsulated RCs. $|d\Phi_D(T)/dT|$ and $|d\Phi_L(T)/dT|$ for (*C*) bulk solvent RCs and (*D*) TMOS encapsulated RCs.

scale, this would imply an unrealistically large shift of the tightly bound cofactors within the protein matrix. By contrast, studies on the variation of the X-band ESP spectra of the $P^{\cdot+}Q_A^{\cdot-}$ secondary radical pair in Q_B-depleted, Zn^{2+}-reconstituted RCs of *Rb. sphaeroides* R26 when cooled in the dark and under illumination revealed only slight modifications of the cofactor arrangement (van den Brink et al., 1994). Small conformational changes depending on the illumination history were also observed for the special pair (Müh et al., 1997) and the photoactive bacteriopheophytin of the RC of *Rb. sphaeroides* (Müh et al., 1998) by means of ENDOR/TRIPLE spectroscopy.

A simple mapping of the rate coefficients on the edge-to-edge distance between donor and acceptor cannot neither account for the complex temperature dependence of the $P^+Q_A^-$ recombination rate coefficients reported by a large number of studies on wild-type and cofactor-modified RCs (Parson, 1967; Gunner et al., 1986; Gunner and Dutton, 1989; Lin et al., 1994; Allen and Williams, 1995; Ortega et al., 1996; McMahon et al., 1998; Schmid and Labahn, 2000; Xu and Gunner, 2000). In all these studies, the ET kinetics were observed to markedly speed up when cooling the RC samples in the dark, with the most pronounced changes happening around 200 K.

This extraordinary temperature dependence of the ET rates cannot be explained by any theoretical ET model using a temperature-independent parameter set throughout the whole temperature range between 10 and 300 K. Therefore, we had earlier introduced a dynamic model in which thermally activated protein fluctuations and relaxations adiabatically vary the intrinsic ET parameters (McMahon et al., 1998). This model was successful in quantitatively describing the temperature dependence of the $P^+Q_A^-$ charge recombination kinetics; i.e., the shapes of the observed rate distributions and not only the average rates. Moreover, comparison of ET kinetics data from both light-cooled and dark-cooled RC samples yielded a consistent picture of protein relaxations on both the neutral and charge-separated energy surfaces, as depicted in Fig. 1. Additional support for a dynamic model comes from other studies, for instance by electron spin echo envelope modulation spectroscopy (ESEEM) of spin-polarized $P^{\cdot+}Q_A^{\cdot-}$ radical pairs (Dzuba et al., 1997), where abrupt changes of the linewidth of the Fourier-transformed ESEEM spectra were explained by stepwise motion of the protein on a multidimensional energy landscape.

Here we have shown that this analysis can be applied to wild-type RCs in both cryosolvent and in a silica hydrogel, showing that charge solvation occurs efficiently in the gel matrix. Large-scale motions, however, are affected in encapsulated RCs. Before continuing with a discussion of the effects of the rigid silica environment on model parameters governing long-range ET, we briefly mention two additional dynamic effects that are outside of the framework of our analysis:

1. At the lowest temperatures, there is clear evidence of the presence of light-induced conformational transitions that also affect the ET rate. These motions are well known from spectral hole-burning studies (Reddy et al., 1992).
2. Above 250 K, we observe a rather weak increase in the average rate in bulk solvent (Fig. 4 *A*). This feature is likely related to temperature- and pH-dependent proton uptake (Kálmán and Maróti, 1994; Maróti and Wraight, 1997). Interestingly, this effect is absent in the TMOS sample; a thorough analysis, however, is outside the scope of this study.

Microscopic ET parameters determined for bulk solvent and TMOS encapsulated RCs

The microscopic parameters governing long-range ET, the electronic coupling V, the energy gap ε, and the reorganization energy λ are difficult to disentangle from experimental

data. Even with temperature-dependent measurements, the separation of ε and λ is problematic because it is their difference that governs the rate coefficient in the Marcus equation, Eq. 5. Previous studies of charge recombination kinetics in RCs with altered primary acceptor (Gunner et al., 1986; Gunner and Dutton, 1989; Allen and Williams, 1998) or with modified P/P^+ midpoint potentials (Ortega et al., 1996; Lin et al., 1994; Dutton and Mosser, 1994; Schmid and Labahn, 2000) used a small number of discrete vibrational modes to model the temperature dependence of the ET kinetics (Jortner, 1976). The temperature-dependencies were associated with changes of λ, ranging from $\approx$600 meV at cryogenic temperature to $\approx$900 meV at room temperature. Similar results were also inferred from electric field modulation experiments (Franzen and Boxer, 1993).

Our interpretation of the temperature and illumination history dependence of the microscopic rate coefficients of $P^+Q_A^-$ recombination is based on a self-consistent mapping of the transfer rate onto a single conformational coordinate (McMahon et al., 1998). The temperature-independent ET parameters are extracted from an analysis of the shapes of the rate distributions and their temperature variations in accordance with the spin boson model. We assume a temperature-independent spectral density $J(\omega)$ of the phonons involved in the ET reaction and thus a constant reorganization energy λ. Both λ and V are determined simultaneously from the ET kinetics. Moreover, the analysis of the temperature dependence of the rate distributions obtained from the ET kinetics enables us to determine $J(\omega)$.

The present work was done on wild-type, carotenoid-containing RCs. The results are in good agreement with those previously published for RCs from the carotenoid-deficient strain R26 (McMahon et al., 1998). There are slight deviations that we attribute to the substantially improved precision of the spin boson calculations rather than differences between the proteins. Whereas it was previously necessary to restrict the *FC* calculations to phonon frequencies below 400 cm^{-1}, we were able to extend the range up to 3400 cm^{-1} in the present analysis. The spectral density $J(\omega)$ obtained in this analysis is similar to previously published results (McMahon et al., 1998). In both cases, $J(\omega)/\omega$ was dominated by a Lorentzian with a half-width of 60 cm^{-1}. Previously, however, this Lorentzian had to be supplemented by additional low-frequency Gaussians (up to 250 cm^{-1}). We found this unnecessary when calculating with the extended phonon spectrum. Classical molecular dynamics simulations of the energy difference between the charge-separated and the neutral state of the ET reaction from the excited special pair to the bacteriopheophytin, $P_S \rightarrow H_L$ (Xu and Schulten, 1992, 1994; Schulten and Tesch, 1991), yielded an exponential energy correlation function with a decay time of 94 fs, which corresponds to a Lorentzian-shaped $J(\omega)/\omega$ with half-width 56.4 cm^{-1}, in excellent agreement with our result. This Lorentzian shape comprises all the low-frequency normal modes, which are delocalized over the entire protein matrix (Gō et al., 1983; Levitt et al., 1985; Smith, 1991).

Our experimental results and the MD simulations are at variance with other reports that invoke significant contributions of localized chromophore vibrations to $P^+Q_A^-$ charge recombination, for instance the carbonyl stretch $\sim$1600 cm^{-1} (Gunner et al., 1986; Gunner and Dutton, 1989; Ortega et al., 1996). Characteristic modes at intermediate frequencies below 1600 cm^{-1} were also employed to fit ET kinetics (Lin et al., 1994; Schmid and Labahn, 2000). In the analysis presented here, the dispersion in the ET kinetic data, as quantified by the sum of pair differences $\Delta_p(t)$ in Eq. 12, proved to be a sensitive tool for determining the overall shape of the spectral density. Of course, slight variations of the parameters characterizing $J(\omega)/\omega$ will remain unnoticed in $\Delta_p(t)$, but high-frequency modes contributing beyond 10% to the total reorganization energy can definitely be excluded.

Setting the free energy gap at room temperature to 510 meV, we have calculated a reorganization energy $\lambda \approx 600$ meV (Table 1), 10% less than the value reported for RCs of the carotenoid lacking strain R26 (McMahon et al., 1998). For the electronic coupling matrix element between charge-separated and charge-recombined state room temperatures, we have obtained $V = 1.70 \times 10^{-4}$ cm^{-1} for bulk solvent RCs, which is also close to the value obtained for R26 RCs (McMahon et al., 1998).

The reliability of the parameter determination procedure is emphasized by its success to also describe charge recombination of RCs encapsulated in a sol-gel matrix. The ET rate is by a factor of two smaller than in bulk solvent at 300 K, but it is not clear, a priori, which control parameter is responsible for the reduced rate. It is well known that the free energy gap between the oxidized special pair, P^+, and the reduced primary acceptor, Q_A^-, is sensitive to changes in the protein environment. P/P^+ midpoint potentials in different solutions range from 453 meV to 520 meV (Arata and Parson, 1981; Moss et al., 1991; Lin et al., 1994; Kong et al., 1998), depending on the experimental approach. Recently, Paschenko and co-workers published a study of the effect of cryosolvents on the P/P^+ midpoint potential. Both the addition of glycerol and DMSO increased the midpoint potential by $\approx$10% as compared with buffer (pH 7.5) (Paschenko et al., 2001). However, such small changes are clearly not sufficient to explain the twofold reduction of the charge recombination rate in TMOS samples.

Although we cannot exclude minor changes of the midpoint potential upon TMOS encapsulation, we have used the same 300-K free energy gap of 510 meV also for TMOS encapsulated RCs. The analysis of the dispersion of the ET kinetics of light-cooled RCs encapsulated in TMOS then yields a reorganization energy of $\lambda = 600$ meV, which is 7 meV higher than the value obtained for RCs in solution. This almost perfect agreement between two independent measurements lends further credence to our conclusion that the overall RC structure is basically unaffected by the

hydrogel. In the classical picture, λ is connected to the dielectric properties of the medium supporting ET (Marcus and Sutin, 1985). Therefore, we can conclude that the macroscopic dielectric properties of the protein in the two environments are essentially identical.

Besides the reorganization energy λ, also the free energy gaps between the $P^+Q_A^-$ and PQ_A potential surface in both light- and dark-adapted conformations are basically identical for the two preparations. Table 2 shows that the center positions of the low-temperature $g(\varepsilon)$ distributions in the light-adapted conformation remain near the 300 K value, as expected from the temperature dependence of the average rates in Fig. 4. Moreover, the $g(\varepsilon)$ distributions of the dark-adapted species are shifted to higher energies by nearly the same amount, 113 (bulk solvent) and 115 meV (TMOS gel). The widths of the distributions are, however, significantly wider for the TMOS samples. We conclude that the sample heterogeneity is significantly larger in the TMOS samples, but both ε and the λ are not sensitive to variation of the protein environment.

By contrast, the electronic coupling matrix element V is an intrinsic sensor for slight modifications of the arrangement of the cofactors. At room temperature, we obtain an electronic coupling of $V = 1.17 \times 10^{-4}$ cm^{-1} for RCs embedded in TMOS, which is 30% less than the value of $V = 1.70 \times 10^{-4}$ cm^{-1} for bulk solvent RCs. We discuss this difference in the context of the empirical expression frequently used to approximate the distance dependence of the electronic coupling between redox partners,

$$V^2 \propto \exp(-\beta d). \tag{23}$$

Here, β is a factor characterizing the decay of the electronic wavefunctions and d the edge-to-edge distance between redox partners (Moser et al., 1992, 1995; Page et al., 1999). With $\beta = 1.4$ Å^{-1}, as obtained experimentally from a number of different ET reactions in proteins (Moser et al., 1992), a twofold reduction of the ET rate coefficient would imply an increase of the spatial separation of both redox partners of ≈0.5 Å. Such a significant displacement of the special pair and Q_A cofactor appears unrealistic. Moreover, such large static deformations of the protein should also affect the protein relaxations, which are not dependent on whether the RCs are in solution or encapsulated in the silica hydrogel.

Therefore, we associate the predominant contribution to the change of the electronic coupling matrix element with the decay parameter β. At a distance of 25 Å between P^+ and Q_A^-, an increase of β by 0.03 Å^{-1} would cause the observed twofold decrease of V^2. This variation reflects the subtle influence of different environments on the donor-acceptor electronic coupling. Beratan and Onuchic have developed a model for ET in proteins with multiple electron tunneling pathways (Beratan et al., 1991, 1992). Each individual pathway consists of through-bond and through-space segments with different distance dependencies. For example, for charge recombination from the primary acceptor in RCs of *Rh. viridis*, the dominant pathway consists of 18 through-bond steps, together with a through-space distance of ≈9 Å (Curry et al., 1995). Quantum interference among the individual pathways plays a crucial role, leading to a pronounced sensitivity of the electronic coupling on slight modifications of the secondary and tertiary structure of the protein matrix (Curry et al., 1995). Indeed, a recent theoretical study has suggested that the pronounced asymmetry of primary charge separation in bacterial photosynthetic RCs can be explained by mutual destructive interferences of different ET pathways between the special pair and the accessory bacteriochlorophyll B_B in the B-branch, causing a reduction of V^2 by three orders of magnitude from the value obtained for the photoactive A-branch (Kolbasov and Scherz, 2000). Moreover, the interference pattern among different electron tunneling pathways can be modulated by thermal motions of the protein. Balabin and Onuchic recently pointed out that dynamical amplification of ET plays a central role if the dominant tunneling pathways interfere destructively (Balabin and Onuchic, 2000). Indeed, for the TMOS hydrogel, in which large-scale protein motions are suppressed (vide infra), we find a smaller electronic coupling matrix element.

From our analysis, we suggest that subtle rearrangements of the co-factors in the TMOS hydrogel matrix, which do not alter ε and λ significantly, slightly affect the shapes, symmetries, and relative orientations of the interacting electronic states. Furthermore, restricted protein motions may enhance destructive interference of tunneling pathways. The result is a detuning of the ET system leading to a twofold slower ET reaction than in the bulk solvent sample.

Structural heterogeneity and conformational relaxation

Nonexponential ET kinetics, as observed here for charge recombination from the primary acceptor in both bulk solvent and TMOS encapsulated RCs, is prevalent also in other ET steps in bacterial photosynthetic RCs (Kirmaier and Holten, 1990; Jia et al., 1993). Following our earlier work (McMahon et al., 1998), we have mapped the continuous distribution of rate coefficients onto a distribution of free energy gaps between the oxidized special pair P^+ and the reduced quinone Q_A^-, thus accounting for the inhomogenous broadening of the system using a single conformational coordinate. Note that the coupling of ε and V through Eq. 10 implicitly introduces a distribution in the electronic coupling as well.

There is ample evidence of distributed energy gaps between redox partners in various steps of bacterial photosynthetic ET. The decay of the excited special pair, P^*, of wild-type and mutant RCs of *Rhodobacter capsulatus* is nonexponential at cryogenic and room temperatures (Jia et al., 1993). Inhomogeneities of the radical pair energies

were observed in delayed fluorescence measurements of the lifetime of $P^+H_A^-$ and magnetic field-dependent reaction yield spectroscopy of the excited triplet state of the special pair (Ogrodnik et al., 1994; Volk et al., 1995). Moreover, light-induced FTIR difference spectra in RCs of *Rh. viridis* (Breton et al., 1999) and *Rb. sphaeroides* (Breton et al., 1997) revealed several conformations of the 10a-ester C=O of the bacteriopheophytin H_A, which cause energetic heterogeneity in the ET steps involving H_A.

The relaxation functions in Fig. 11 that were derived from the temperature dependence of the energy gaps show a number of discrete steps, representing dynamic processes that become activated in different temperature ranges and thus correspond to thermally activated transitions in different tiers of the hierarchy of conformational substates (Frauenfelder et al., 1991; Nienhaus and Young, 1996). Our experiments cannot access the lowest tier, CS3, properly because transitions at this level can be both light-induced and thermally induced. The next steps, which are designated as CS2 and CS1 in Fig. 11, *A* and *B*, are present in both solution and TMOS samples. The separation is quite pronounced in the solution sample on the slow (hour) timescale of the annealing of the light-cooled sample, but less evident in TMOS. Note that the distinction between CS2 and CS1 vanishes entirely on the 100-ms relaxation timescale of the dark-cooled sample. This relaxation process shifts with the glass transition of the solvent (McMahon, 1997), and consequently, motions in this tier are coupled to the solvent dynamics. In our previous study, we exploited the different timescales of the observed relaxations, $\approx$100 ms for the dark-cooled sample and $\approx 10^4$ s for the light-cooled one, to obtain the thermal activation parameters of the different steps, using either the Arrhenius or Ferry relation. The Arrhenius Law,

$$\kappa(T) = A_A \frac{T}{T_0} \exp[-E_A/k_B T], \tag{24}$$

applies to a thermally activated transition over a one-dimensional barrier of height E_A, where A_A is a pre-exponential factor, T is the absolute temperature, T_0 is a reference temperature (which we take to be 100 K), and k_B the Boltzmann constant. In systems where cooperative transitions are involved, for instance proteins and viscous solvents, Ferry's Law (Ferry et al., 1953; Frauenfelder and Wolynes, 1994),

$$\kappa(T) = A_F \exp[-(E_F/k_B T)^2], \tag{25}$$

often provides a better description of the temperature dependence of the rate coefficients. In Eq. 25, the parameter E_F has the interpretation of a roughness scale characterizing a multiminimum rugged energy landscape governing the dynamics. In our previous work (McMahon et al., 1998), we showed that the analysis of the CS1 and CS0 steps gave physically more reasonable parameters when using the Ferry relation, which suggested that these two steps are characterized by cooperative dynamics. To understand the nature of CS2, we quote an interesting relation which connects the cooperative dynamics in a viscous solvent with the average Arrhenius energy barrier, $\langle E_A \rangle$, below the glass transition temperature, T_g (Richert and Bässler, 1990),

$$\langle E_A \rangle = E_F^2/k_B T_g. \tag{26}$$

With $E_F = 7.8$ kJ/mol for CS1 and $T_g \approx 170$ K, we estimate $\langle E_A \rangle \approx 43$ kJ/mol, which is similar to the 50 kJ/mol from the experimental determination (McMahon et al., 1998). Therefore, we believe that the CS2 step is not really a separate level in the substate hierarchy, but rather a different manifestation of the CS1 dynamics below the dynamic transition temperature. The poorly separated CS2 and CS1 steps in TMOS compared with bulk solvent (compare Fig. 11, *A* and *B*) are reasonable in view of the larger degree of heterogeneity in the TMOS sample, which is expected to smear out the transition temperature. This larger heterogeneity is also evident from the markedly broader peak in $|d\Phi/dT|$ of the dark-cooled sample (see Fig. 11, *C* and *D*).

The step at the highest temperature (CS0) was previously associated with large-scale conformational changes (McMahon et al., 1998). This separate feature is missing in the silica hydrogel RC preparation, implying that the silica matrix suppresses these motions. Further evidence of the limited ability of the RCs to fluctuate comes from the room temperature kinetics. For bulk solvent RCs, we observe exponential recombination within the error of our data. A single apparent rate coefficient $\langle k_{ET} \rangle$ is observed if the protein ensemble samples the entire conformational space q during the lifetime of the charge-separated state. For RCs embedded in a sol-gel matrix, a distribution of rate coefficients persists up to room temperature, which is clear evidence of a heterogeneous ensemble on the timescale of charge separation. Although we cannot prove it, the heterogeneity likely persists on all timescales because the proteins are locked in different conformations in the matrix. This interpretation is further supported by studies of geminate and bimolecular recombination of CO to wild-type and β93 modified hemoglobin trapped in sol-gel matrices. Under these conditions, hemoglobin is arrested in a particular quaternary structure in the silica matrix (Khan et al., 2000, 2001).

In a study complementary to our temperature-dependent investigations, Cordone and co-workers recently changed the solvent viscosity to slow conformational fluctuations in RCs by using different amounts of trehalose (Palazzo et al., 2002). They observed a pronounced broadening of the lifetime distributions of the charge-separated state upon increasing the trehalose content in the buffer beyond 70% (wt). This behavior is expected if the timescales of internal protein fluctuations that cause an averaging of the kinetics are governed by solvent viscosity. Drastic changes were observed above 90% trehalose, where the sample turned into

a solid trehalose glass. With conformational dynamics completely arrested in the trehalose matrix, relaxation from the dark-adapted state to the light-adapted state is no longer possible, and in accordance with our dynamic model, the ET rate was observed to increase to its value in the dark-adapted state (Palazzo et al., 2002).

In summary, we have presented a comparative analysis of the temperature dependence of RCs in cryosolvent and in a silica matrix. Using an elaborate analysis based on the spin boson model, we were able to explore the differences in the dynamic behavior between the two environments. In the immobilized sample, local conformational changes occur, similar as in solution. Larger structural rearrangements are, however, suppressed in the rigid silica matrix. The restriction of protein motions may also be responsible for the observed reduction in the electronic coupling matrix element of the TMOS sample.

APPENDIX: THE SPIN BOSON MODEL

The spin boson model is widely used to describe the dynamics of a two-state system coupled to a heat bath, which is represented by a set of harmonic oscillators (Leggett et al., 1987). In the case of charge recombination kinetics in photosynthetic RCs, the two states are the charge-separated ($P^+Q_A^-$) state and the neutral or charge-recombined (PQ_A) state.

Here we give a brief summary of the considerations leading to analytical expressions that allow us to compute ET rates numerically. Assuming that the interaction between system and environment are linear in both system and environment coordinates, the spin boson Hamiltonian can be split into an electronic part, $\mathcal{H}_{el}$, a part describing the bath, $\mathcal{H}_{osc}$, and a coupling term, $\mathcal{H}_{coupl}$,

$$\mathcal{H}_{SB} = \mathcal{H}_{el} + \mathcal{H}_{osc} + \mathcal{H}_{coupl} \tag{27}$$

with

$$\mathcal{H}_{el} = V\sigma_x + \frac{1}{2}\varepsilon\sigma_z, \tag{28}$$

$$\mathcal{H}_{osc} = \sum_\alpha \left(\frac{p_\alpha^2}{2m_\alpha} + \frac{1}{2} m_\alpha \omega_\alpha^2 x_\alpha^2 \right), \tag{29}$$

$$\mathcal{H}_{coupl} = \frac{1}{2}\sigma_z \sum_\alpha c_\alpha x_\alpha, \tag{30}$$

where σ_x and σ_z denote the Pauli spin matrices,

$$\sigma_x = \begin{pmatrix} 0 & 1 \\ 1 & 0 \end{pmatrix} \quad \text{and} \quad \sigma_z = \begin{pmatrix} 1 & 0 \\ 0 & -1 \end{pmatrix}. \tag{31}$$

V is the electronic coupling matrix element between the charge-separated and charge-recombined state, and $\hbar$ denotes Planck's constant. The coupling strength between each harmonic oscillator and the electron transition is quantified by the parameter c_α. A sufficient characterization of the environment is given by the spectral density,

$$J(\omega) = \frac{\pi}{2} \sum_\alpha \frac{c_\alpha^2}{m_\alpha \omega_\alpha} \delta(\omega - \omega_\alpha). \tag{32}$$

There are numerous methods of computing the survival probability of the charge-separated state, $P(t) = \langle \sigma_z(t) \rangle$, under different conditions, like time-dependent perturbation theory (Leggett et al., 1987), path integral approaches (Chakravarty and Leggett, 1984; Chang and Chakravarty, 1985; Garg et al., 1985; Onuchic et al., 1986; Leggett et al., 1987; Onuchic, 1987), and Monte-Carlo path integral simulations (Egger and Mak, 1994a,b; Egger et al., 2000).

For weak electronic coupling V and moderate coupling to the environment, an exponential decay, $P(t) = \exp[-kt]$, would be expected, with a rate coefficient k identical to the result of time-dependent perturbation theory for nonadiabatic ET. This behavior can be derived self-consistently in the framework of the noninteracting blip approximation (Chakravarty and Leggett, 1984; Chang and Chakravarty, 1985; Garg et al., 1985; Onuchic et al., 1986; Leggett et al., 1987; Onuchic, 1987). For any system coupled to a dissipative environment, the probability, $p(x_f;t)$, to reach a final coordinate x_f at time t in configuration space, irrespective of the state of the environment, can be calculated by the path integral expression (Feynman and Vernon Jr., 1963)

$$p(x_f;t) = \int \mathcal{D}x(\tau) \int \mathcal{D}y(\tau') \mathcal{A}[x(\tau)] \mathcal{A}^\dagger[y(\tau')] \times \mathcal{F}[x(\tau), y(\tau')], \tag{33}$$

where $x(\tau)$ and $y(\tau)$ denote trajectories in configuration space, $\mathcal{A}[x(\tau)]$ is the amplitude of the system to follow $x(\tau)$ without any coupling to the environment, and $F[x(\tau), y(\tau')]$ is the influence functional describing the coupling between system and environment. For an environment represented by harmonic oscillators, $F[x(\tau), y(\tau')]$ can be calculated analytically (Feynman and Vernon Jr., 1963). In our concrete example of an electron transfer step coupled to the environment, the variables $x(\tau)$ and $y(\tau)$ can only take the values assigned to the potential minima of the reactant and product state, respectively, leading to four discrete states for the pair $[x(\tau), y(\tau')]$. They are lumped together in the reduced density matrix,

$$\varrho = \begin{pmatrix} A & B \\ C & D \end{pmatrix}. \tag{34}$$

The diagonal elements A and D represent the system being in either the reactant or the product state, referred to as sojourns, whereas the off-diagonal ones B and C, the so-called blips, describe a system undetermined between the reactant and product state. The latter two states, therefore, represent destruction of phase coherence by the dissipative environment. As the amplitude for switching between A and D during the time interval dt is $i\,V/\hbar\,dt$, the survival probability $P(t)$ of the charge-separated state can be expressed in a power series expansion of V^2,

$$P(t) = \sum_{n=0}^{\infty} (-1)^n V^{2n} K_n(t). \tag{35}$$

The influence functional, which is contained in the coefficients $K_n(t)$, decomposes into four factors representing interactions between adjacent sojourns and blips as well as self-interaction terms, which have to be derived from the exact path integral formulation Eq. 33. In the noninteracting blip approximation, interactions between adjacent blips are neglected, leading to a substantial simplification of the formalism. The survival probability $P(t)$ can be computed via its Laplace transform $\tilde{P}(\lambda)$

$$\tilde{P}(\lambda) = \int dt \exp[-\lambda t] P(t) = \frac{1 - \dfrac{\tilde{h}(\lambda)}{\lambda}}{\lambda + \tilde{g}(\lambda)}, \tag{36}$$

with

$$\tilde{h}(\lambda) = \left(\frac{2V}{\hbar} \right)^2 \int dt \exp(-\lambda t) \sin\left(\frac{\varepsilon t}{\hbar} \right) \sin\left(\frac{Q_1(t)}{\pi\hbar} \right) \times \exp\left[-\frac{Q_2(t,T)}{\pi\hbar} \right], \tag{37}$$

$$\tilde{g}(\lambda) = \left(\frac{2V}{\hbar}\right)^2 \int dt \exp(-\lambda t)\cos\left(\frac{\varepsilon t}{\hbar}\right)\sin\left(\frac{Q_1(t)}{\pi\hbar}\right) \times \exp\left[-\frac{Q_2(t,T)}{\pi\hbar}\right]. \quad (38)$$

The functions $Q_1(t)$ and $Q_2(t, T)$ are given by

$$Q_1(t) = \int_0^\infty d\omega \frac{J(\omega)/\omega}{\omega}\sin(\omega t), \quad (39)$$

$$Q_2(t,T) = 2\int_0^\infty d\omega \frac{J(\omega)/\omega}{\omega}\sin^2\left(\frac{\omega t}{2}\right)\coth\left(\frac{\hbar\omega}{2k_BT}\right). \quad (40)$$

The self-consistency relation for the noninteracting blip approximation requires that the power series expansions of $\tilde{g}(\lambda)$ and $\tilde{h}(\lambda)$ can be truncated after the first term (Chakravarty and Leggett, 1984; Chang and Chakravarty, 1985; Leggett et al., 1987),

$$g_1 = \lim_{\lambda\to 0}\frac{d\tilde{g}(\lambda)}{d\lambda} \ll 1. \quad (41)$$

Finally, the incoherent decay rate k is given by the well-known expression

$$k \equiv g_0 = \left(\frac{2V}{\hbar}\right)^2 \int_0^\infty dt \cos\left(\frac{\varepsilon t}{\hbar}\right)\sin\left(\frac{Q_1(t)}{\pi\hbar}\right)\exp\left[-\frac{Q_2(t,T)}{\pi\hbar}\right], \quad (42)$$

which we have evaluated numerically to analyze the data presented in this article.

Here we will show that the self-consistency criterion, Eq. 41, is fulfilled in the case of long-range ET in the photosynthetic RC, independent of the spectral density $J(\omega)$. This is done by examining the asymptotic behavior of the integrand of $\tilde{g}(\lambda)$ and thus the asymptotic behavior of $Q_1(t)$ and $Q_2(t, T)$. As an upper limit, it is sufficient to consider the case $T = 0$. If the derivatives of $J(\omega)/\omega$ do not vanish for $\omega \to 0$, the asymptotic behavior of $Q_1(t)$ and $Q_2(t, T = 0)$ is given by

$$Q_1(t) = \sqrt{\frac{j_1^3}{j_3}}\arctan\left(\sqrt{\frac{j_1}{j_3}}\,t\right) + \mathcal{O}\left(\frac{1}{t^4}\right) \quad \text{for} \quad t \to \infty \quad (43)$$

and

$$Q_2(t, T=0) = \frac{j_0}{2}\ln\left(1 + \frac{j_0 t^2}{j_2}\right) + \mathcal{O}\left(\frac{1}{t^3}\right) \quad \text{for} \quad t \to \infty. \quad (44)$$

Here, the j_i terms are defined as

$$j_i := \left[\left(\frac{d}{d\omega}\right)^i \frac{J(\omega)}{\omega}\right]_{\omega=0}, \quad i = 0, 1, 2, 3. \quad (45)$$

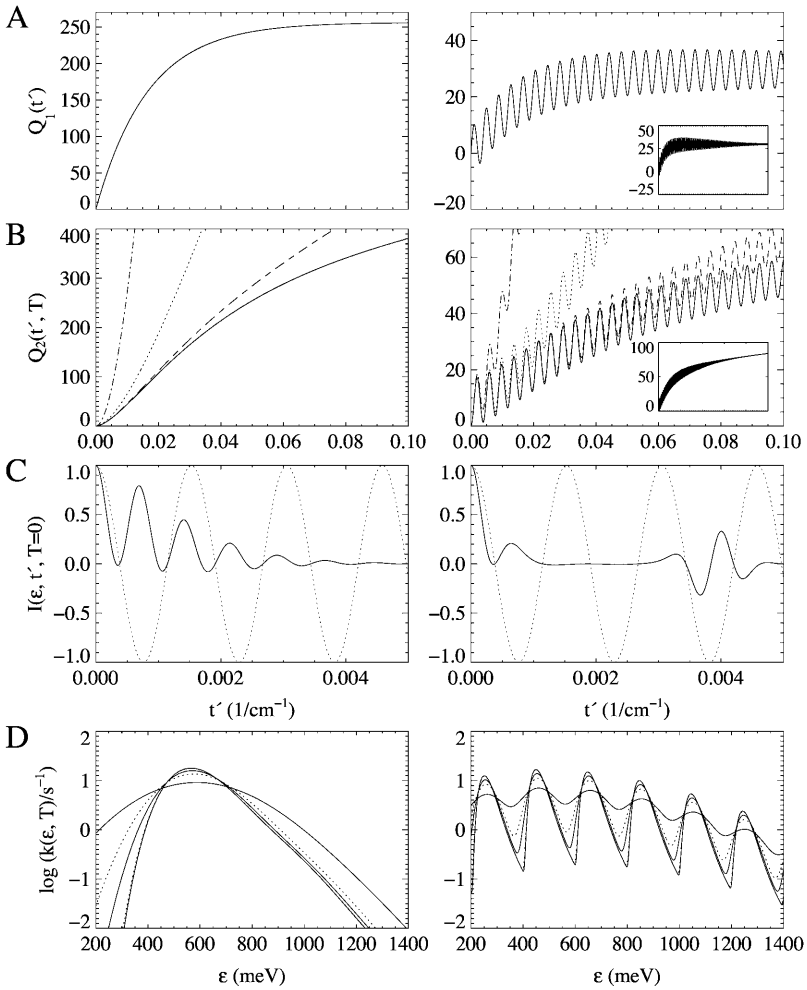

FIGURE 12 Numerical computation of *FC*s using the experimentally determined spectral density (*left*) and a spectral density with a high-frequency component contributing 90% to the total reorganization energy (ω_S = 60 cm^{-1}, ω_{high} = 1600 cm^{-1}, and σ_{high} = 7 cm^{-1}, *right*). In both cases, the reorganization energy is λ = 600 meV. (*A*) $Q_1(t')$; (*B*) $Q_2(t', T)$ for $T = 0$ (*solid line*), 10 (*dashed line*), 100 (*dotted line*), and 300 K (*dash-dotted line*); (*C*) integrand $I(\varepsilon, t')$ of Eq. 42 for ε = 500 meV and $T = 0$ (*dotted line* = cos $\varepsilon t'$); and (*D*) $k(\varepsilon, T)$ for 0, 5, 10, 50, 100, and 300 K (alternating *solid* and *dotted lines*). The insets in *A* and *B* illustrate the asymptotic behavior of $Q_1(t')$ and $Q_2(t', T = 0)$. $Q_1(t')$ and $Q_2(t', T)$ are given in units of $\hbar$. Note that t is substituted by $t' = t/\hbar$, with t' given in inverse wavenumbers (1/cm^{-1}). For comparison: t' = 1/cm^{-1} corresponds to t = 5.3 ps.

These expressions reproduce the long-time behavior of $Q_1(t)$ and $Q_2(t, T)$ in the special case of an ohmic spectral density, i.e. $J(\omega) \propto \omega \exp(-\omega/\omega_c)$ (Leggett et al., 1987). It is straightforward to show that

$$g_1 = \mathcal{O}\left(\frac{V^2}{\varepsilon^2}\right). \quad (46)$$

In bacterial photosynthetic RCs, $\varepsilon \approx 500$ meV and $V \approx 2 \times 10^{-5}$ meV for charge recombination from the primary acceptor Q_A. Thus, the self-consistency relation is safely fulfilled, and the microscopic rate coefficient k can safely be calculated with Eq. 42.

The physical meaning of the individual terms in this equation can be understood from the path integral formalism based on Eq. 33. For linear coupling between the system and the environment, the influence functional can be written as (Feynman and Vernon Jr., 1963)

$$\mathcal{F}[x(\tau), y(\tau')] = e^{\mathbf{i}\Phi[x(\tau), y(\tau')]}. \quad (47)$$

The influence phase $\Phi[x(\tau), y(\tau')]$ can be expressed in terms of the functions $Q_1(t)$, which describes the classical response of the environment to a force $f(t) = \delta(t)$ for $t > 0$, and $Q_2(t, T)$, which represents thermal fluctuations of the ensemble of harmonic oscillators. Each of the oscillators is characterized by its mean occupation number, $\tilde{n} = (\exp[\hbar\omega/k_B T] - 1)^{-1}$. The factor $\cos(\varepsilon t/\hbar)$ corresponds to the bare amplitude, $A[x(\tau)]$, of the system for staying in either the charge-separated or charge-recombined state, respectively. Finally, V^2 originates from the amplitude for a transition between both states.

In our analysis, we have parameterized the spectral density $J(\omega)$ heuristically by a small number of discrete components. The first, Lorentzian term in Eq. 8 represents a Debye-like dielectric response of the solvent and protein matrix surrounding the redox pair upon charge separation (Rips and Jortner, 1987). Gaussians are also included to account for vibrational contributions. In general, they can be nonlocal low frequency modes, as generally observed in proteins (Gō et al., 1983; Smith, 1991), or localized modes of the cofactors coupled to the ET reaction.

Unlike the Marcus equation, Eq. 5, which is only valid in the classical, high temperature limit, the spin boson model takes the quantum nature of excitations in the condensed phase into account. From studying ET rates as a function of energy gap ε and temperature T, spectral densities can be determined which represent the dependence of the dynamics of the two-state system on specific properties of the environment.

To illustrate the influence of different spectral densities on the various terms in Eq. 42, we consider two physically interesting cases: 1) Debye response, as obtained from our data, i.e., all Gaussian amplitudes $S_i = 0$; and 2) a high frequency mode at 1600 cm^{-1} dominating the spectral density. Fig. 12 shows plots of the functions $Q_1(t)$, $Q_2(t, T)$, the integrand $I(\varepsilon, t, T)$ of Eq. 42, and the microscopic rate coefficients $k(\varepsilon, T)$ for both cases. Parameters of the two model densities are included in the caption of Fig. 12.

Pure dielectric relaxation (case 1) results in a monotonic behavior of the functions $Q_1(t)$ and $Q_2(t, T)$ (Fig. 12, *A* and *B*) and thus generates a smooth dependence of the microscopic rate coefficients $k(\varepsilon, T)$ and the redox energy, peaking close to $\varepsilon = \lambda$ (Fig. 12 *D*). The high-frequency dominated spectral density (Fig. 12, *right*), exhibits oscillatory behavior in $k(\varepsilon, T)$, with the highest rates occurring at redox energies in resonance with the vibrational energy. This effect was also reported by Gunner and co-workers (Gunner et al., 1986; Gunner and Dutton, 1989), who applied a quantum-corrected Marcus-type expression for nonadiabatic ET (Levich and Doganadze, 1959; Jortner, 1976) with a small number of discrete modes coupling to the ET, and by Onuchic who investigated a small number of modes coupled to a dissipative environment (Onuchic, 1987). Note the echo in $I(\varepsilon, t', T = 0)$ observed after an initial decay that is directly related to the periodic behavior of the thermal fluctuations of the bath bosons in $Q_2(t, T)$ (Fig. 12 *B*). Such damped revivals are typical of quantum systems interacting with a bath of bosons (e.g., Schleich, 2001; and references therein). These examples show the flexibility of the spin boson model to model a variety of situations by a suitable parameterization of the spectral density $J(\omega)$, provided that the self-consistency relation (Eqs. 41 and 46) is satisfied.

We thank Prof. S. G. Boxer, Stanford University, for his kind gift of the SMpHis strain of *Rhodobacter sphaeroides*-producing His-tagged reaction centers.

This work was supported by the Volkswagen Foundation and the Deutsche Forschungsgemeinschaft (Sonderforschungsbereich 569).

REFERENCES

Allen, J. P., G. Feher, T. O. Yeates, H. Komiya, and D. C. Rees. 1987. Structure of the reaction center from *Rhodobacter sphaeroides* R-26: the cofactors. *Proc. Natl. Acad. Sci. USA.* 84:5730–5734.

Allen, J. P., and J. C. Williams. 1995. Relationship between the oxidation potential of the bacteriochlorophyll dimer and electron transfer in photosynthetic reaction centers. *J. Bioenerg. Biomembr.* 27:275–283.

Allen, J. P., and J. C. Williams. 1998. Photosynthetic reaction centers. *FEBS Lett.* 438:5–9.

Arata, H., and W. W. Parson. 1981. Delayed fluorescence from *Rhodopseudomonas sphaeroides* reaction centers. Enthalpy and free energy changes accompanying electron transfer from *P*-870 to quinones. *Biochim. Biophys. Acta.* 638:201–209.

Balabin, I. A., and J. N. Onuchic. 2000. Dynamically controlled protein tunneling paths in photosynthetic reaction centers. *Science.* 290:114–117.

Beratan, D. N., J. N. Betts, and J. N. Onuchic. 1991. Protein electron transfer rates set by the bridging secondary and tertiary structure. *Science.* 252:1285–1288.

Beratan, D. N., J. N. Betts, and J. N. Onuchic. 1992. Tunneling pathway and redox-state dependent electronic couplings at nearly fixed distance in electron-transfer proteins. *J. Phys. Chem.* 96:2852–2855.

Breton, J., M. Bibikova, D. Oesterhelt, and E. Nabedryk. 1999. Conformational heterogeneity of the bacteriopheophytin electron acceptor H_A in reaction centers from *Rhodopseudomonas viridis* revealed by Fourier transform infrared spectroscopy and site-directed mutagenesis. *Biochemistry.* 38:11541–11552.

Breton, J., E. Nabedryk, J. P. Allen, and J. C. Williams. 1997. Electrostatic influence of Q_A reduction on the IR vibrational mode of the 10a-ester C=O of H_A demonstrated by mutations at residues Glu L104 and Trp L100 in reaction centers from *Rhodobacter sphaeroides*. *Biochemistry.* 36:4515–4525.

Brinker, C. J., and G. W. Scherer. 1990. Sol-Gel Science. The Physics and Chemistry of Sol-Gel Processing. Academic Press, New York.

Chakravarty, S., and A. Leggett. 1984. Dynamics of the two-state system with ohmic dissipation. *Phys. Rev. Lett.* 52:5–8.

Chang, L. D., and S. Chakravarty. 1985. Dissipative dynamics of a two-state system coupled to a heat bath. *Phys. Rev. B.* 31:154–164.

Chen, K. C., T. Tsuchiya, and J. D. Mackenzie. 1986. Sol-gel processing of silica: I. The role of the starting compounds. *J. Non-Cryst. Sol.* 81: 227–237.

Clayton, R. K., and W. R. Sistrom, editors. 1978. The Photosynthetic Bacteria. Plenum Press, New York.

Curry, W. B., M. D. Grabe, I. V. Kurnikov, S. S. Skourtis, D. N. Beratan, J. J. Regan, A. J. Aquino, P. Beroza, and J. N. Onuchic. 1995. Pathways, pathway tubes, pathway docking, and propagators in electron transfer proteins. *J. Bioenerg. Biomembr.* 27:285–293.

Dutton, P. L., and C. C. Mosser. 1994. Quantum biomechanics of long-range electron transfer in protein: hydrogen bonds and reorganization energies. *Proc. Natl. Acad. Sci. USA.* 91:10247–10250.

Dzuba, S. A., P. Gast, and A. J. Hoff. 1997. Probing the energy landscape of bacterial photosynthetic reaction centers at cryogenic temperatures by ESEEM of spin-polarised $D^+Q_A^-$ radical pairs. *Chem. Phys. Lett.* 268: 273–279.

Egger, R., and C. H. Mak. 1994a. Low-temperature dynamical simulation of spin-boson systems. *Phys. Rev. B*. 50:15210–15220.

Egger, R., and C. H. Mak. 1994b. Quantum rates for nonadiabatic electron transfer. *J. Chem. Phys*. 100:2651–2660.

Egger, R., L. Mühlbacher, and C. H. Mak. 2000. Path-integral Monte Carlo simulations without the sign problem: multilevel blocking approach for effective actions. *Phys. Rev. E*. 61:5961–5966.

Ellerby, L. M., C. R. Nishida, F. Nishida, S. A. Yamanaka, B. Dunn, J. S. Valentine, and J. I. Zink. 1992. Encapsulation of proteins in transparent porous silicate glasses prepared by the sol-gel method. *Science*. 255:1113–1115.

Ermler, U., G. Fritzsch, S. K. Buchanan, and H. Michel. 1994. Structure of the photosynthetic reaction centre from *Rhodobacter sphaeroides* at 2.65 Å resolution: cofactors and protein-cofactor interactions. *Structure*. 2: 925–936.

Feher, G., J. P. Allen, M. Y. Okamura, and D. C. Rees. 1989. Structure and function of bacterial photosynthetic reaction centers. *Nature*. 339:111–116.

Ferry, J. D., L. D. Grandine, Jr., and E. R. Fitzgerald. 1953. The relaxation distribution function of polyisobutylene in the transition from rubber-like to glass-like behavior. *J. Appl. Phys*. 24:911–916.

Feynman, R. P., and F. L. Vernon, Jr. 1963. The theory of a general quantum system interacting with a linear dissipative system. *Ann. Phys*. 24:118–173.

Franzen, S., and S. G. Boxer. 1993. Temperature dependence of the electric field modulation of electron transfer rates: charge recombination in photosynthetic reaction centers. *J. Phys. Chem*. 97:6304–6318.

Frauenfelder, H., S. G. Sligar, and P. G. Wolynes. 1991. The energy landscapes and motions of proteins. *Science*. 254:1598–1603.

Frauenfelder, H., and P. G. Wolynes. 1994. Biomolecules: where the physics of complexity and simplicity meet. *Phys. Tod*. 47:58–64.

Ganago, A. O., A. Y. Shkuropatov, and V. A. Shuvalov. 1991. Subpicosecond dynamics of excited state of primary electron donor in reaction centers of *Rhodopseudomonas viridis* as revealed by hole burning at 1.7 K broad and narrow holes. *FEBS Lett*. 284:199–202.

Garg, A., J. N. Onuchic, and V. Ambegaokar. 1985. Effect of friction on electron transfer in biomolecules. *J. Chem. Phys*. 83:4491–4503.

Gill, I., and A. Ballesteros. 1998. Encapsulation of biologicals within silicate, siloxane, and hybrid sol-gel polymers: an efficient and generic approach. *J. Am. Chem. Soc*. 120:8587–8598.

Gill, I., and A. Ballesteros. 2000a. Bioencapsulation within synthetic polymers (part 1): sol-gel encapsulated biologicals. *Trends Biotechnol*. 18:282–296.

Gill, I., and A. Ballesteros. 2000b. Bioencapsulation within synthetic polymers (part 2): non-sol-gel protein-polymer composites. *Trends Biotechnol*. 18:469–479.

Gō, N., T. Noguti, and T. Nishikawa. 1983. Dynamics of a small globular protein in terms of low-frequency vibrational modes. *Proc. Natl. Acad. Sci. USA*. 80:3696–3700.

Goldsmith, J. O., and S. G. Boxer. 1996. Rapid isolation of bacterial photosynthetic reaction centers with an engineered poly-histidine tag. *Biochim. Biophys. Acta*. 1276:171–175.

Gottfried, D. S., A. Kagan, B. M. Hoffmann, and J. M. Friedman. 1999. Impeded rotation of a protein in a sol-gel matrix. *J. Phys. Chem. B*. 103:2803–2807.

Gray, H. B., and B. G. Malmström. 1989. Long-range electron transfer in multisite metalloproteins. *Biochemistry*. 28:7499–7505.

Gray, H. B., and J. R. Winkler. 1996. Electron transfer in proteins. *Annu. Rev. Biochem*. 65:537–561.

Gunner, M. R., and P. L. Dutton. 1989. Temperature and $-\Delta G^0$ dependence of the electron transfer from Bph^- to Q_A in reaction center protein from *Rhodobacter sphaeroides* with different quinones as Q_A. *J. Am. Chem. Soc*. 111:3400–3412.

Gunner, M. R., D. E. Robertson, and P. L. Dutton. 1986. Kinetic studies on the reaction center protein from *Rhodopseudomonas sphaeroides*: the temperature and free energy dependence of electron transfer between various quinones in the Q_A site and the oxidized bacteriochlorophyll dimer. *J. Phys. Chem*. 90:3783–3795.

Hoff, A. J., and J. Deisenhofer. 1997. Photophysics and photosynthesis. Structure and spectroscopy of reaction centers of purple bacteria. *Phys. Rep*. 287:1–247.

Jia, Y., T. J. DiMagno, C. Chan, Z. Wang, M. Du, D. K. Hanson, M. Schiffer, J. R. Norris, G. R. Fleming, and M. S. Popov. 1993. Primary charge separation in mutant reaction centers of *Rhodobacter capsulatus*. *J. Phys. Chem*. 97:13180–13191.

Jortner, J. 1976. Temperature-dependent activation energy for electron transfer between biological molecules. *J. Chem. Phys*. 64:4860–4867.

Kálmán, L., and P. Maróti. 1994. Stabilization of reduced primary quinone by proton uptake in reaction centers of *Rhodobacter sphaeroides*. *Biochemistry*. 33:9237–9244.

Khan, I., D. Dantsker, U. Samuni, A. J. Friedman, C. Bonaventura, B. Manjula, S. A. Acharya, and J. M. Friedman. 2001. β93 modified hemoglobin: kinetic and conformational consequences. *Biochemistry*. 40:7581–7592.

Khan, I., C. F. Shannon, D. Dantsker, A. J. Friedman, J. Apodaca, and J. M. Friedman. 2000. Sol-gel trapping of functional intermediates of hemoglobin: geminate and bimolecular recombination studies. *Biochemistry*. 39:16099–16109.

Kirmaier, C., and D. Holten. 1990. Evidence that a distribution of bacterial reaction centers underlies the temperature and detection-wavelength dependence of the rates of the primary electron-transfer reactions. *Proc. Natl. Acad. Sci. USA*. 87:3552–3556.

Kleinfeld, D., M. Y. Okamura, and G. Feher. 1984. Electron-transfer kinetics in photosynthetic reaction centers cooled to cryogenic temperatures in the charge-separated state: evidence for light-induced structural changes. *Biochemistry*. 23:5780–5786.

Kolbasov, D., and A. Scherz. 2000. Asymmetric electron transfer in reaction centers of purple bacteria strongly depends on different electron matrix elements in the active and inactive branches. *J. Phys. Chem. B*. 104:1802–1809.

Kong, J., Z. Lu, Y. M. Lvov, R. Z. B. Desamero, H. A. Frank, and J. F. Rusling. 1998. Direct electrochemistry of cofactor redox sites in a bacterial photosynthetic reaction center. *J. Am. Chem. Soc*. 120:7371–7372.

Leggett, A., S. Chakravarty, A. T. Dorsey, M. P. A. Fisher, and A. Garg. 1987. Dynamics of the dissipative two-state system. *Rev. Mod. Phys*. 59:1–85.

Levich, V. G., and R. R. Doganadze. 1959. Teoriya bezizluchatelnikh electronnikh perekhodov mezhdu ionami v rastvorakh. *Dokl. Acad. Nauk. SSSR*. 124:123–126.

Levitt, M., C. Sander, and P. S. Stern. 1985. Protein normal-mode dynamics: trypsin inhibitor, crambin, ribonuclease and lysozyme. *J. Mol. Biol*. 181:423–447.

Lin, X., H. A. Murchison, V. Nagarajan, W. W. Parson, J. P. Allen, and J. C. Williams. 1994. Specific alteration of the oxidation potential of the electron donor in reaction centers from *Rhodobacter sphaeroides*. *Proc. Natl. Acad. Sci. USA*. 91:10265–10269.

Livage, J., T. Coradin, and C. Roux. 2001. Encapsulation of biomolecules in silica gels. *J. Phys. Condens. Matter*. 13:R673–R691.

Marcus, R. A. 1964. Chemical and electrochemical electron-transfer theory. *Annu. Rev. Phys. Chem*. 15:155–196.

Marcus, R. A., and N. Sutin. 1985. Electron transfers in chemistry and biology. *Biochim. Biophys. Acta*. 811:265–322.

Maróti, P., and C. A. Wraight. 1997. Kinetics of H^+ ion binding by the $P^+Q_A^-$ state of bacterial photosynthetic reaction centers: rate limitation within the protein. *Biophys. J*. 73:367–381.

McMahon, B. H. 1997. Energetics of protein fluctuations: ligand binding to myoglobin and electron transfer in reaction center. PhD thesis. University of Illinois at Urbana-Champaign.

McMahon, B. H., J. D. Müller, C. A. Wraight, and G. U. Nienhaus. 1998. Electron transfer and protein dynamics in the photosynthetic reaction center. *Biophys. J*. 74:2567–2587.

Miller, J. M., B. Dunn, J. S. Valentine, and J. I. Zink. 1996. Synthesis conditions for encapsulating cytochrome *c* and catalase in SiO_2 sol-gel materials. *J. Non-Cryst. Sol.* 202:279–289.

Moser, C. C., J. M. Keske, K. Warncke, R. S. Farid, and P. L. Dutton. 1992. Nature of biological electron transfer. *Nature.* 355:796–802.

Moser, C. C., C. C. Page, R. Farid, and P. L. Dutton. 1995. Biological electron transfer. *J. Bioenerg. Biomembr.* 27:263–274.

Moss, D. A., M. Leonhard, M. Bauscher, and W. Mäntele. 1991. Electrochemical redox titration of cofactors in the reaction center from *Rhodobacter sphaeroides*. *FEBS Lett.* 283:33–36.

Müh, F., J. Rautter, and W. Lubitz. 1997. Two distinct conformations of the primary electron donor in reaction centers from *Rhodobacter sphaeroides* revealed by ENDOR/TRIPLE-spectroscopy. *Biochemistry.* 36:4155–4162.

Müh, F., C. Schulz, E. Schlodder, M. R. Jones, J. Rautter, M. Kuhn, and W. Lubitz. 1998. Effects of zwitterionic detergents on the electronic structure of the primary donor and the charge recombination kinetics of $P^+Q_A^-$ in native and mutant reaction centers from *Rhodobacter sphaeroides*. *Photosyn. Res.* 55:199–205.

Nienhaus, G. U., and R. D. Young. 1996. Protein dynamics. *In* Encyclopedia of Applied Physics, Vol. 15. 163–184.

Noks, P. P., E. P. Lukashev, A. A. Kononenko, P. S. Venediktov, and A. B. Rubin. 1977. Possible role of macromolecular components in the functioning of photosynthetic reaction centers of purple bacteria. *Mol. Biol. (Mosk.).* 11:1090–1099.

Ogrodnik, A., W. Keupp, M. Volk, G. Aumeier, and M. E. Michel-Beyerle. 1994. Inhomogeneity of radical pair energies in photosynthetic reaction centers revealed by differences in recombination dynamics from $P^+H_A^-$ when detected in delayed emission and absorption. *J. Phys. Chem.* 98:3432–3439.

Okamura, M. Y., R. A. Isaacson, and G. Feher. 1975. Primary acceptor in bacterial photosynthesis: obligatory role of ubiquinone in photoactive reaction centers of *Rhodopseudomonas spheroides*. *Proc. Natl. Acad. Sci. USA.* 72:3491–3495.

Onuchic, J. N. 1987. Effect of friction on electron transfer: the two reaction coordinate case. *J. Chem. Phys.* 86:3925–3943.

Onuchic, J. N., D. N. Beratan, and J. J. Hopfield. 1986. Some aspects of electron-transfer reaction dynamics. *J. Phys. Chem.* 90:3707–3721.

Ortega, J. M., P. Mathis, J. C. Williams, and J. P. Allen. 1996. Temperature dependence of the reorganization energy for charge recombination in the reaction center from *Rhodobacter sphaeroides*. *Biochemistry.* 35:3354–3361.

Page, C. C., C. C. Moser, X. Chen, and P. L. Dutton. 1999. Natural engineering principles of electron tunnelling in biological oxidation-reduction. *Nature.* 402:47–52.

Palazzo, G., A. Mallardi, A. Hochkoeppler, L. Cordone, and G. Venturoli. 2002. Electron transfer kinetics in photosynthetic reaction centers embedded in trehalose glasses: trapping of conformational substates at room temperature. *Biophys. J.* 82:558–568.

Parson, W. W. 1967. Flash-induced absorbance changes in *Rhodospirillum rubrum* chromatophores. *Biochim. Biophys. Acta.* 131:154–172.

Paschenko, V. Z., P. P. Knox, S. K. Chamorovsky, P. M. Krasilnikov, M. D. Mamedov, A. Y. Semenov, N. I. Zakharova, G. Renger, and A. B. Rubin. 2001. Effect of D_2O and cryosolvents on the redox properties of bacteriochlorophyll dimer and electron transfer processes in *Rhodobacter sphaeroides* reaction centers. *Bioelectrochemistry.* 53:233–241.

Peloquin, J. M., J. C. Williams, X. Lin, R. G. Alden, A. K. Taguchi, J. P. Allen, and N. W. Woodbury. 1994. Time-dependent thermodynamics during early electron transfer in reaction centers from *Rhodobacter sphaeroides*. *Biochemistry.* 33:8089–8100.

Reddy, N. R. S., P. A. Lyle, and G. J. Small. 1992. Application of spectral hole burning spectroscopies to antenna and reaction center complexes. *Photosyn. Res.* 31:167–194.

Richert, R., and H. Bässler. 1990. Dynamics of supercooled melts treated in terms of the random-walk concept. *J. Phys. Condens. Matter.* 2:2273–2288.

Rips, I., and J. Jortner. 1987. Dynamic solvent effects on outer-sphere electron transfer. *J. Chem. Phys.* 87:2090–2104.

Rubin, A. B., A. A. Kononenko, K. V. Shaitan, V. Z. Paschenko, and G. Y. Riznichenko. 1994. Electron transport in photosynthesis. *Biofizika.* 39: 173–195.

Schleich, W. P. 2001. Quantum Optics in Phase Space. Wiley-VCH, Weinheim.

Schmid, R., and A. Labahn. 2000. Temperature and free energy dependence of the direct charge recombination rate from the secondary quinone in bacterial reaction centers from *Rhodobacter sphaeroides*. *J. Phys. Chem.* 104:2928–2936.

Schulten, K., and M. Tesch. 1991. Coupling of protein motions to electron transfer: molecular dynamics and stochastic quantum mechanics study of photosynthetic reaction centers. *Chem. Phys.* 158:421–446.

Sharp, K. A. 1998. Calculation of electron transfer reorganization energies using the finite difference Poisson-Boltzmann model. *Biophys. J.* 74: 1241–1250.

Shibayama, N., and S. Saigo. 1995. Fixation of the quaternary structures of human adult haemoglobin by encapsulation in transparent porous silica gels. *J. Mol. Biol.* 251:203–209.

Smith, J. C. 1991. Protein dynamics: comparison of simulations with inelastic neutron scattering experiments. *Q. Rev. Biophys.* 24:227–291.

Steinbach, P. J., K. Chu, H. Frauenfelder, J. B. Johnson, D. C. Lamb, G. U. Nienhaus, T. B. Sauke, and R. D. Young. 1992. Determination of rate distributions from kinetic experiments. *Biophys. J.* 61:235–245.

Tess, M. E., and J. A. Cox. 1999. Chemical and biochemical sensors based on advances in materials chemistry. *J. Pharm. Biomed. Anal.* 19:55–68.

van Brederode, M. E. 1999. New pathways for ultrafast electron transfer in photosynthetic reaction centers of *Rhodobacter sphaeroides*. PhD thesis. Vrije Universiteit Amsterdam.

van den Brink, J. S., H. Manikowski, P. Gast, and A. J. Hoff. 1994. Temperature-dependent electron spin polarization of the triplet state of the primary donor in *Rhodopseudomonas viridis*. *Biochim. Biophys. Acta.* 1185:177–187.

Volk, M., A. Ogrodnik, and M. E. Michel-Beyerle. 1995. The recombination dynamics of the radical pair P^+H^- in external and magnetic fields. *In* Anoxygenic Bacteria. R. E. Blankenship, M. T. Madigan, and C. E. Bauer, editors. Kluwer Academic Publishers, Dordrecht. 595–626.

Warshel, A., Z. T. Chu, and W. W. Parson. 1989. Dispersed polaron simulations of electron transfer in photosynthetic reaction centers. *Science.* 246:112–116.

Warshel, A., and J.-H. Hwang. 1986. Simulation of the dynamics of electron transfer reactions in polar solvents: semiclassical trajectories and dispersed polaron approaches. *J. Chem. Phys.* 84:4938–4957.

Woodbury, N. W., and W. W. Parson. 1986. Nanosecond fluorescence from chromatophores of *Rhodopseudomonas sphaeroides* and *Rhodospirillum rubrum*. *Biochim. Biophys. Acta.* 850:197–210.

Xu, D., and K. Schulten. 1992. Multi-mode coupling of protein motions to electron-transfer in the photosynthetic reaction center: spin-boson theory based on a classical molecular dynamics simulation. *In* The Photosynthetic Reaction Center II. J. Breton, and A. Verméglio, editors. Plenum Press, New York. 301–312.

Xu, D., and K. Schulten. 1994. Coupling of protein motion to electron transfer in a photosynthetic reaction center: investigating the low temperature behavior in the framework of the spin-boson model. *Chem. Phys.* 182:91–117.

Xu, Q., and M. R. Gunner. 2000. Temperature dependence of the free energy, enthalpy, and entropy of $P^+Q_A^-$charge recombination in *Rhodobacter sphaeroides* R-26 reaction centers. *J. Phys. Chem.* 104: 8035–8043.